

# 1 Dynamics of Variable Dusk-Dawn Flow Associated with Magnetotail 2 Current Sheet Flapping

3  
4 James H. Lane<sup>1</sup>, Adrian Grocott<sup>1</sup>, Nathan A. Case<sup>1</sup>, Maria-Theresia Walach<sup>1</sup>

5  
6 <sup>1</sup> Department of Physics, Lancaster University, Lancaster, UK

7  
8 Correspondence to: James Lane ([j.lane@lancaster.ac.uk](mailto:j.lane@lancaster.ac.uk))

9  
10

## 11 Abstract

12 ~~We present Cluster spacecraft observations from 12 October 2006 of convective plasma~~  
13 ~~flows in the Earth's magnetotail. Earthward flow bursts with a dawnward  $v_{1,y}$  component,~~  
14 ~~observed by Cluster 1 (C1), are inconsistent with the duskward flow that might be expected~~  
15 ~~at the pre-midnight location of the spacecraft. Previous observations have suggested that~~  
16 ~~the dusk-dawn sense of the flow can be governed by the Interplanetary Magnetic Field~~  
17 ~~(IMF)  $B_y$  conditions, with the related 'untwisting hypothesis' of magnetotail dynamics~~  
18 ~~commonly invoked to explain this dependence, in terms of a large-scale magnetospheric~~  
19 ~~asymmetry. In the current study, observations of the upstream solar wind conditions from~~  
20 ~~OMNI, magnetic field observations by Cluster, and ionospheric convection data using~~  
21 ~~SuperDARN, indicate a large-scale magnetospheric morphology consistent with positive IMF~~  
22  ~~$B_y$  penetration into the magnetotail. At the pre-midnight location of Cluster, however, the~~  
23 ~~dawnward flow observed below the neutral sheet by C1 could only be explained by the~~  
24 ~~untwisting hypothesis in a negative IMF  $B_y$  scenario. The Cluster magnetic field data also,~~  
25 ~~reveal a flapping of the magnetotail current sheet; a phenomenon known to influence dusk-~~  
26 ~~dawn flow. Results from the curlometer analysis technique suggest that the dusk-dawn~~  
27 ~~sense of the  $\mathbf{J} \times \mathbf{B}$  force was consistent with localized kinks in the magnetic field and the~~  
28 ~~flapping associated with the transient perturbations to the dusk-dawn flow observed by C1.~~  
29 ~~We therefore suggest that the flapping overcame the dusk-dawn sense of the large-scale~~  
30 ~~convection which we would expect to have been net duskward in this case. We conclude~~  
31 ~~that invocation of the untwisting hypothesis may be inappropriate when interpreting~~

Formatted: Font: Not Bold

Deleted: We present Cluster spacecraft observations from 12 October 2006 of convective plasma flows in the Earth's magnetotail. Earthward flow bursts with a dawnward  $v_{1,y}$  component, observed by Cluster 1 (C1), are inconsistent with the duskward flow that might be expected at the pre-midnight location of the spacecraft.

Deleted: suggested that

Deleted: of of both slow ( $< 200 \text{ km s}^{-1}$ ) and fast ( $> 200 \text{ km s}^{-1}$ ) convective magnetotailthe

Deleted: is strongly

Deleted: , with . The

Deleted: I

Deleted: o

Deleted: During this interval, observations

Deleted: magnetic field observations by Cluster,

Deleted: . At the pre-midnight location of Cluster, however,

Deleted: by C1 could only be explained by the untwisting hypothesis in a negative IMF  $B_y$  scenario

Deleted: . Inspection of the in-situ Cluster magnetic field

Deleted: Cluster magnetic field

Deleted: data

Deleted: s

Deleted: the

Deleted: luster

Deleted: spacecraft

Deleted: We suggest that the

Deleted: therefore

Deleted: flapping overcame the dawn-dusk

Deleted: large-scale which we would expect to have been net duskward in this case.

62 intervals of dynamic magnetotail behaviour such as during current sheet flapping,  
63 particularly at locations where magnetotail flaring becomes dominant.

64

## 65 **1. Introduction**

66

67 Convective magnetotail plasma flows at Earth, driven by the closing of magnetic flux via  
68 reconnection as part of the Dungey Cycle (Dungey, 1961) have been studied extensively for  
69 many years (e.g. Angelopoulos et al. 1992, 1994; Sergeev et al., 1996; Petrukovich et al.,  
70 2001; Cao et al., 2006; McPherron et al., 2011; Frühauff & Glassmeier, 2016). Arguably, the  
71 most well studied of these is the Bursty Bulk Flow (BBF). Angelopoulos et al. (1994) defined  
72 BBFs as being channels of earthward plasma flow continually above  $100 \text{ km s}^{-1}$ , exceeding  
73  $400 \text{ km s}^{-1}$  at one point across some interval, usually across a timescale of a few minutes.  
74 The flows are said to be the main transporter of mass, energy and flux in the magnetotail  
75 (e.g. Angelopoulos et al., 1994; Nakamura et al., 2002; Grocott et al., 2004a; Kiehas et al.,  
76 2018). Although their earthward nature is the key defining characteristic of BBFs, they will  
77 invariably exhibit a dusk-dawn component in their bulk flow as well (e.g. Angelopoulos et  
78 al., 1994; Petrukovich et al., 2001; Grocott et al., 2004b). Understanding the drivers of dusk-  
79 dawn asymmetries in magnetospheric dynamics is an important element of geospace  
80 research (e.g. Haaland et al., 2017).

81

82 Magnetotail flows are generally expected to be symmetric about midnight (e.g. Kissinger et  
83 al., 2012). A key factor that has been observed to influence the dusk-dawn direction of the  
84 magnetotail flow, however, is the  $B_y$  component of the Interplanetary Magnetic Field (IMF).  
85 It is well established that when the IMF reconnects with the dayside terrestrial magnetic  
86 field, a non-zero IMF  $B_y$  component leads to asymmetric loading of open flux into the polar  
87 cap (e.g. Khurana et al., 1996; Tenfjord et al., 2015; Grocott et al., 2017; Ohma et al., 2019).  
88 This results in a twisting of the magnetotail whereby the closed field lines are rotated about  
89 the midnight meridian, and a  $B_y$  component is superimposed onto the tail field as a  
90 consequence of IMF  $B_y$  penetration (Cowley, 1981; Petrukovich, 2011; Tenfjord et al., 2015).  
91 Subsequently, following nightside reconnection, the tail will untwist (Grocott et al., 2004c),  
92 with the excitation of multiple convective flow bursts, each with an earthward and dusk-  
93 dawn component, in the tail and nightside ionosphere (Grocott et al., 2007). In order to be

Deleted: , at least in the absence of any asymmetry

95 consistent with the tail ‘untwisting hypothesis’, any convective flows associated with an  
96 individual tail field line should share the same dusk-dawn direction (e.g. see Figure 3 of  
97 Grocott et al., 2005). The role of IMF  $B_y$  in the untwisting hypothesis has been examined  
98 previously in a number of studies (e.g. Grocott et al, 2007; Pitkänen et al., 2013, 2015,  
99 2017). These studies revealed that under prolonged positive IMF  $B_y$  conditions, the  
100 earthward flows are expected to exhibit a dawnward component in the northern  
101 hemisphere ( $B_x > 0$ ) and a duskward component in the southern hemisphere ( $B_x < 0$ ), with  
102 the opposite correlation for negative IMF  $B_y$  conditions. This is especially true close to  
103 midnight, where the penetration of IMF  $B_y$  is particularly noticeable. Further away from  
104 midnight, however, effects such as magnetotail flaring (Fairfield, 1979) are expected to  
105 product a dominant  $B_y$  component, which may suppress IMF  $B_y$ -effects on the dusk-dawn  
106 asymmetry, resulting in the symmetric earthward convection of field lines (e.g. see Fig. 2 of  
107 Pitkänen et al., 2019). Nevertheless, IMF  $B_y$  has been shown to govern the dusk-dawn  
108 nature of these flows both during periods of steadier, slower convection (Pitkänen et al.,  
109 2019), as well as during more transient, dynamic BBF-like intervals (Grocott et al., 2007) at  
110  $|Y_{GSM}|$  values up to  $7 R_E$  (Pitkänen et al., 2013). In the present study, we present Cluster  
111 observations of dawnward and duskward directed flows that do not match this expected  
112 dependence on IMF  $B_y$ , implying that the untwisting hypothesis is insufficient in this case. In  
113 particular, we highlight the problematic nature of the observation of dawnward flow, in  
114 relation to the pre-midnight location of Cluster. We instead suggest that the flows are being  
115 driven by local perturbations due to dynamic behaviour of the tail that are associated with  
116 flapping of the current sheet.

117  
118 The current sheet, or ‘neutral’ sheet, lies in the equatorial plane at the center of the tail  
119 plasma sheet and separates the earthward ( $B_x > 0$ ) and tailward ( $B_x < 0$ ) directed field (Ness,  
120 1965). The current sheet is a highly dynamic region of the Earth’s magnetotail which can  
121 undergo various types of net motion, such as tilting due to lobe magnetic pressures (Cowley  
122 et al., 1981; Tenfjord et al., 2017) as well as flapping. Flapping of the current sheet can  
123 generally be described as a sinusoidal-like variation in  $B_x$  of up to tens of nanoTesla, where  
124 an observing spacecraft often measures repeated changes in the sign of  $B_x$  (e.g. Runov et al.,  
125 2009), indicative of crossings of the current sheet, with characteristic times ranging from a  
126 few seconds to (more commonly) several minutes (e.g. Runov et al., 2009; Wu et al., 2016;

Deleted: towards the dusk-dawn flanks

128 Wei et al., 2019). Drivers of current sheet flapping have been widely investigated, with  
129 possible causes ranging from external solar wind/IMF changes (Runov et al., 2009),  
130 induction of hemispheric plasma asymmetries (Malova et al., 2007; Wei et al., 2015), fast  
131 earthward flow (Nakamura et al., 2009) as well as periodical, unsteady magnetotail  
132 reconnection (Wei et al., 2019). Studies such as Volwerk et al. (2008) and Kubyshkina et al.  
133 (2014) have illustrated that flapping of the current sheet can be associated with variable  
134 dusk-dawn flow, potentially overriding, or preventing any IMF  $B_y$  control of the flow.

135  
136 In this paper we present Cluster spacecraft observations of an interval of dynamic  
137 magnetotail behaviour on 12 October 2006, prior to which the  $B_y$  component of the  
138 concurrent upstream IMF had been largely positive for several hours. Throughout this  
139 interval, Cluster 1 observed oscillations in the magnetic field  $B_x$  component, which we  
140 attribute to current sheet flapping, concurrent with a series of convective fast flows with  
141 significant and variable dusk-dawn components. Observations from Cluster 2, 3 and 4  
142 indicated that the spacecraft were at a pre-midnight location where magnetotail flaring was  
143 dominating over IMF  $B_y$  control of the flows, resulting in the expectation of (symmetrical)  
144 duskward return flows (Pitkänen et al., 2019). In the southern hemisphere, such duskward  
145 flow was measured by Cluster 3, but not observed by Cluster 1, which instead measured  
146 flows with significant dawnward components. These dawnward flows were therefore  
147 inconsistent with any expectation that the flow was governed by flaring and, owing to  
148 evidence of large-scale IMF  $B_y > 0$  ionospheric convection pattern, could also not be  
149 explained by the magnetotail untwisting hypothesis. We instead suggest that the current  
150 sheet flapping was exciting the variable dusk-dawn flow, overriding the expected large-scale  
151 duskward convection at the location of Cluster 1.

Deleted: .

Deleted: The  $B_y$  component of the concurrent upstream IMF had been largely positive for several hours prior to the flapping...

Deleted: . Consequently, the interval discussed here provides an opportunity to investigate the possible competition of two distinct mechanisms for control of the dusk-dawn flow: 1) IMF  $B_y$  and 2) localized dynamics related to the flapping of the current sheet. In contrast to studies which have come before such as those presented by Grocott et al. (2007) and Pitkänen et al. (2015), the observed dusk-dawn direction of transient flow enhancements in this case disagrees with that which might be expected from the prevailing IMF  $B_y$  conditions, despite clear evidence for global penetration of positive IMF  $B_y$ .

Deleted: . We therefore suggest that IMF  $B_y$  penetration at the location of Cluster was unable to overcome the variable dusk-dawn flow associated with the flapping.

## 153 2. Instrumentation and Data Sets

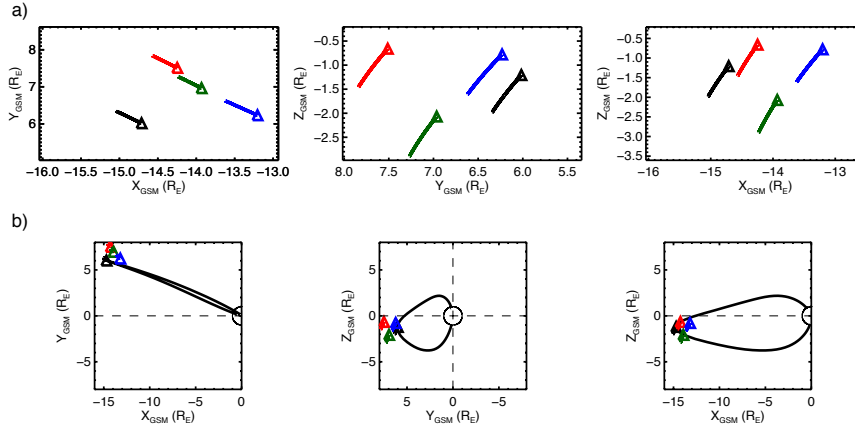
### 154 2.1. Spacecraft Data

155 The magnetospheric observations presented in this case study were made by the Cluster  
156 multi-spacecraft (C1-C4) constellation (Escoubet et al., 2001). We make use of the fluxgate  
157 magnetometer (FGM) onboard the Cluster spacecraft to obtain magnetic field  
158 measurements (Balogh et al., 2001), and obtain our bulk ion velocity data from the Hot Ion  
159 Analyser (HIA) on C1 and C3 calculated as on-board moments (Rème et al., 1997). The

178 magnetic field data presented are 5 vectors-per-second (0.2s res) which have been 1s  
179 median-averaged, with the velocity data presented having spin resolution of just over 4s.  
180 Where these datasets have been combined to produce parameters such as the plasma beta  
181 and field-perpendicular velocities, we have resampled both the magnetic field and plasma  
182 data to 5s resolution. All data are presented in geocentric solar magnetospheric (GSM)  
183 coordinates unless stated otherwise.

184

185 The interval of study in this paper occurred between 00:00 – 00:55 UT on 12 October 2006.  
186 At 00:00 UT the Cluster spacecraft were located in the near-Earth magnetotail plasma sheet,  
187 in the pre-midnight sector. C1 was located at  $(X = -14.7, Y = 6.0, Z = -1.2)$   $R_E$ , C2 at  $(X =$   
188  $-14.2, Y = 7.5, Z = -0.7)$   $R_E$ , C3 at  $(X = -13.9, Y = 7.0, Z = -2.1)$   $R_E$ , and C4 at  $(X = -13.2, Y = 6.2,$   
189  $Z = -0.8)$   $R_E$ . This is depicted in Fig. 1a by the colored triangles, along with the respective  
190 spacecraft trajectories, from 00:00 – 00:55 UT, by the solid lines. Fig. 1b shows a zoomed-  
191 out version of Fig. 1a, which illustrates the location of the spacecraft with respect to the  
192 Earth. Fig. 1b also shows a traced modelled magnetic field line, achieved using the semi-  
193 empirical TA15 model of the magnetosphere (Tsyganenko & Andreeva, 2015), which passes  
194 through the location of C1 and connects to both the northern and southern hemispheres of  
195 the Earth. We parameterised the TA15 model using mean-averaged solar wind dynamic  
196 pressure ( $P_{dyn}$ ), IMF  $B_y$  and IMF  $B_z$  data from the 1-hour interval prior to 00:28 UT (the start  
197 of our specific interval of interest). These values were  $P_{dyn} = 1.56$  nPa, IMF  $B_y = +1.56$  nT and  
198 IMF  $B_z = -2.17$  nT. There was also a tailward dipole tilt of  $\approx -12^\circ$ . The model was also  
199 parameterised with a solar wind coupling function index known as the 'N index', after  
200 Newell et al. (2007). The N index varies between 0 (quiet) and 2 (very active), and in this  
201 instance was  $\sim 0.4$ .



202  
 203 **Figure 1:** a) The locations of the Cluster spacecraft in the X-Y, Y-Z, and X-Z GSM planes, from  
 204 left to right, respectively, at 00:00 UT on 12 October 2006, marked by the triangles. The  
 205 trajectories from 00:00 UT to 00:55 UT are marked by the solid lines. The spacecraft are  
 206 color-coded according to the key on the right. b) As in a), with a zoomed-out view. The Earth  
 207 is shown by the solid circle. A TA15 model magnetic field line passing through the location of  
 208 C1 is shown as the solid black line.

209  
 210 The IMF measurements used in this study were provided by the OMNIweb database at 1-  
 211 minute resolution, having been first propagated from L1 to the bow shock nose (King &  
 212 Papitashvili, 2005).

## 214 2.2. SuperDARN Data

215 The ionospheric observations presented in section 3.3 were provided by the Super Dual  
 216 Auroral Radar Network (SuperDARN), an international collaboration of 36 ground-based  
 217 radars (Nishitani et al., 2019) that make line-of-sight Doppler measurements of the  
 218 horizontal motion of the ionospheric plasma every few seconds (e.g. Chisham et al., 2007).  
 219 Here, we use 2-min ionospheric convection maps created by fitting the line-of-sight  $E \times B$   
 220 velocity data to an eighth order expansion of the ionospheric electric potential in spherical  
 221 harmonics using the technique of Ruohoniemi & Baker (1998), implemented in the Radar  
 222 Software Toolkit (RST version 4.2, 2018). To accommodate intervals with limited data  
 223 availability, the data are supplemented with values derived from a statistical model

224 parameterized by IMF conditions. This is a well-established technique that has been  
225 thoroughly discussed by, e.g., Chisham et al. (2007). The convection maps we present  
226 employ the commonly used model of Ruohoniemi & Greenwald (1996). As a check on the  
227 sensitivity of the maps to the choice of model input, we also tested the fitting using the  
228 alternative model of Thomas and Shepherd (2018) and found that this has little impact on  
229 the maps and no impact on our conclusions.

230

231 As a further measure to ensure that the choice of model is not critical to our results, we  
232 chose not to use the concurrent IMF vector to parameterise the background model. In this  
233 case, because we are using the SuperDARN data to provide evidence in support of the  
234 expected large-scale influence of IMF  $B_y$ , we deemed it inappropriate to include model data  
235 already parametrised by IMF  $B_y$ . We instead specify a nominal southward IMF with zero  $B_y$   
236 component in our analysis, to ensure that a background model with no pre-existing IMF  $B_y$   
237 influence is used. Although this might result in the patterns we show being less accurate  
238 overall, especially in regions of poor data coverage, it will ensure that any  $B_y$ -associated  
239 asymmetry in the maps is driven by the radar data from our interval of study, and not the  
240 background model. This is discussed further in section 4.1, below.

241

### 242 **3 Observations**

243

244 In this section we present observations of the IMF, magnetotail magnetic field and plasma  
245 flow, and ionospheric convection from an interval on 12 October 2006.

246

#### 247 *3.1 IMF Observations*

248 Figure 2 presents an overview of the spacecraft data from an extended interval around our  
249 period of specific interest for broader context. In Figure 2a, we show a time-series of the  
250 IMF  $B_y$  and IMF  $B_z$  data from 20:00 UT on 11 October to 01:00 UT on 12 October 2006. These  
251 data reveal that IMF  $B_y$  was generally positive for several hours prior to the fast flow  
252 interval, with IMF  $B_z$  predominantly negative. There were three small intervals of negative  
253 IMF  $B_y$  at  $\sim 21:35$  UT, 23:00 UT and 23:40 UT and we discuss the possible ramifications of  
254 these, and our treatment of them, in section 4.1.

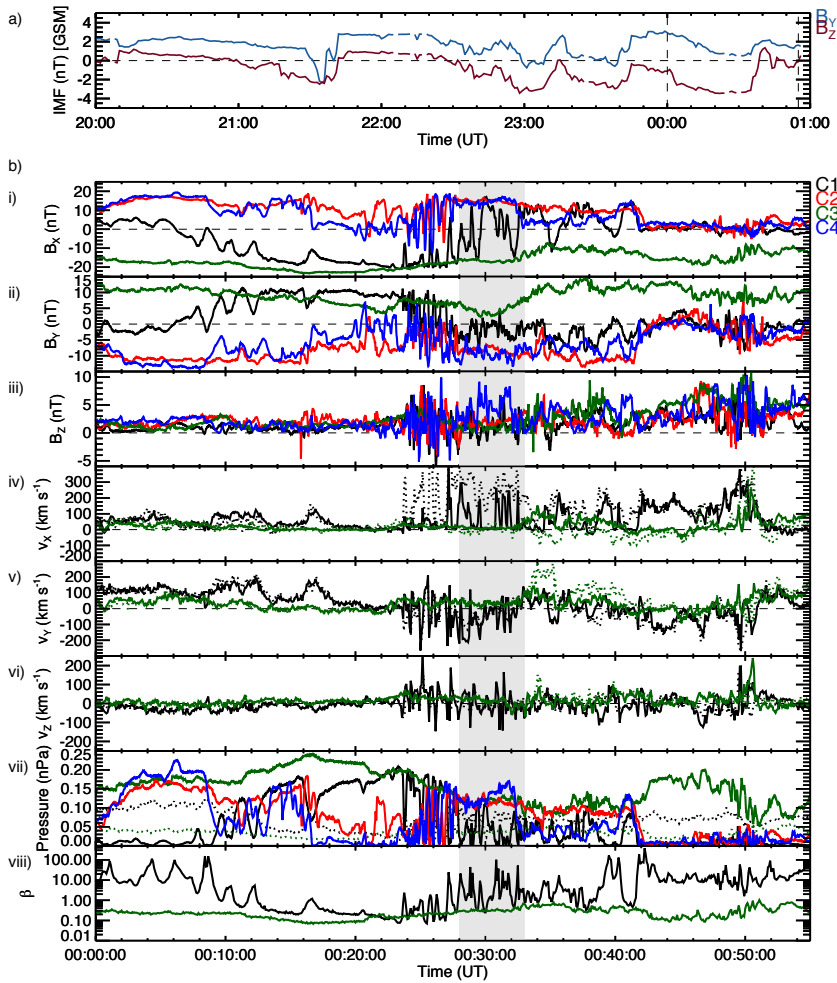
255

256 3.2 Cluster Spacecraft Observations

257 In Figure 2b, we present the in-situ magnetic field and plasma measurements from the

258 Cluster spacecraft across the interval 00:00 – 00:55 UT.

259



260

261 **Figure 2:** a) A plot of the IMF time series data for the IMF  $B_y$  (blue)

262 components, from 20:00 UT on 11 October 2006 to 01:00 UT on 12 October 2006. The

263 vertical dashed lines indicate the start (00:00 UT) and end (00:55 UT) of the interval of



264 Cluster data (below). b) The in-situ Cluster spacecraft measurements. Shown first is the local  
 265 magnetic field data, i)  $B_x$ , ii)  $B_y$  and iii)  $B_z$ , followed by the bulk ion velocity data, iv)  $v_x$ , v)  $v_y$ ,  
 266 and vi)  $v_z$  (dotted lines). The field-perpendicular component of the ion flow (indicative of  
 267 the  $\mathbf{E} \times \mathbf{B}$  convection) is shown in panels iv) to vi) by the solid lines. In panel vii) the magnetic  
 268  $\left(\frac{B^2}{2\mu_0}\right)$  and thermal ion ( $nkT$ ) pressures are shown by the solid and dotted lines respectively,  
 269 and in panel viii) the ion plasma beta from C1 and C3 is shown. All data are labelled  
 270 according to the color-coded key on the right-hand side. The time-interval between the gray  
 271 shaded region marks our specific interval of interest (discussed in text).

272

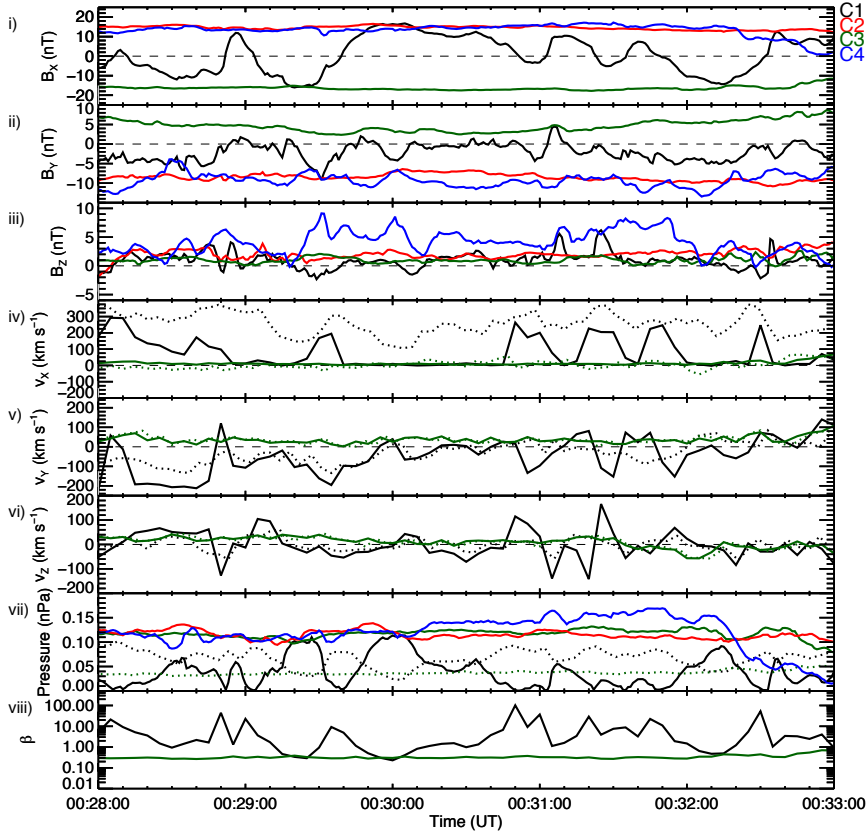
273

274 At ~00:06 UT, C1 crossed from the northern hemisphere into the southern hemisphere,  
 275 illustrated by the sign change in  $B_x$  from positive to negative shown in Fig. 2b i). Coincident  
 276 with this, the observed  $B_y$ , shown in Fig. 2b ii) turned from negative to positive, consistent  
 277 with the expected  $B_y$  due to magnetotail flaring (see section 4.2) at this pre-midnight  
 278 location (Fairfield, 1979). Fig. 2b iv) reveals that up until ~00:24 UT, the bulk earthward flow  
 279 ( $v_x$ , dotted lines) and field-perpendicular flow ( $v_{\perp x}$ , solid lines) measured by both C1 and C3  
 280 was generally low in magnitude ( $< 100 \text{ km s}^{-1}$ ). The dusk-dawn ( $v_y$ ) component of the flow,  
 281 shown in Fig. 2b v), remained steadily duskward ( $v_y > 0$ ) at C1 and duskward or close to zero  
 282 at C3. The north-south ( $v_z$ ) component of the flow in Fig. 2b vi), measured by C1 and C3 was  
 283 effectively zero. During this period, the Cluster spacecraft that resided in the northern  
 284 hemisphere (predominantly C2 and C4), observed  $B_y < 0$ , and the spacecraft which resided  
 285 in the southern hemisphere (predominantly C1 and C3) observed  $B_y > 0$ , again consistent  
 286 with magnetotail flaring. Occasionally a spacecraft encountered the current sheet ( $B_x = 0$ ) at  
 287 which point it observed  $B_y = 0$ . We comment on the significance of these magnetic field  
 288 observations in section 4.2.

289

290 After ~00:24 UT, C1 began to observe a period of enhanced earthward flow  
 291 ( $v_x > 300 \text{ km s}^{-1}$ ) and variable dusk-dawn flow, concurrent with sudden variation in the local  
 292  $B_x$  component. Similarly, C2 and C4, but not C3, observed large magnitude ( $> 20 \text{ nT}$ ) rapid  
 293 variations in  $B_x$ , which appear to have an apparent timescale of around a minute and which  
 294 we attribute to a flapping of the current sheet. As well as rapid variations in  $B_x$ , both the  $B_y$

295 and  $B_z$  components of C1, C2 and C4 seemed highly variable. As perhaps to be expected,  
296 these variations in the magnetic field were accompanied by significant variations in the  
297 magnetic pressure of  $\sim 0.15$  nPa, as shown by the solid lines in Fig. 2b vii).  
298 Unlike the other spacecraft, C3 remained in the southern hemisphere throughout the entire  
299 interval and did not observe the rapid fluctuations in  $B_x$ . Between 00:28 – 00:33 UT (the gray  
300 shaded region), C1 began to repeatedly and rapidly cross the current sheet, as previously  
301 experienced by C2 and C4, whilst continually observing enhanced earthward flow and  
302 variable dusk-dawn convective flow ( $v_{1y}$ ). Across the entire interval, the plasma beta,  $\beta$ ,  
303 indicated in Fig. 2b viii), measured by C3 remained above  $\sim 0.1$ , with C1's measured  $\beta$   
304 ranging from 0.1 to over 100. This is consistent with the fact that C1 was continually  
305 crossing the current sheet at the center of the plasma sheet, where  $\beta$  is larger (Baumjohann  
306 et al., 1989). It is this interval of current sheet crossing and variable flow observed by C1  
307 that we focus on below and is presented in more detail in Figure 3.



308  
309 **Figure 3:** As in Fig. 2b, but for the interval 00:28 – 00:33 UT on 12 October 2006.

310  
311 Fig. 3 i) conveys the extent of the large-amplitude  $B_x$  variations observed by C1 between  
312 00:28 and 00:33 UT.  $B_x$  was generally fluctuating between positive and negative values  
313 throughout the five-minute interval, with a minimum at  $\sim -16$  nT and maximum at  $\sim 17$  nT.  
314 The magnetic pressure at C1 shown by the solid black line in Fig. 3 vii) is consistent with the  
315 idea that C1 was crossing the current sheet, as this generally reached minima at the center  
316 of each current sheet crossing ( $B_x \approx 0$ ). The  $B_y$  component (Fig. 3ii) measured by C1 generally  
317 remained negative and highly variable for the entire interval, with a number of large  
318 negative enhancements and a few small positive excursions. It is particularly of note that  
319 when C1 was below the neutral sheet, as implied by a negative  $B_x$  component,  $B_y$  was

320 almost always negative. As we discuss in section 4.2, this is inconsistent with what we would  
321 expect based on the location of the spacecraft and also inconsistent with any expectation  
322 that a positive IMF  $B_y$  should have penetrated into the tail. The  $B_z$  component (Fig. 3iii)  
323 generally remained positive with some small negative excursions.

324

325 Unlike C1, C2-4 measured generally steady  $B_x$  throughout this five-minute period. C2 and C4  
326 measured positive  $B_x$ , indicating that they were above the neutral sheet, and C3 measured  
327 negative  $B_x$ , indicating that it was below the neutral sheet. Similarly,  $B_y$  was steadily negative

328 for C2 and C4 and steadily positive for C3. These observations are consistent with the larger-

329 scale  $B_y$  at the spacecraft location being dominated by magnetotail flaring. Again, we note

330 the inconsistency between the C1 and C3 observations of  $B_y$ ; when in the southern

331 hemisphere C1 generally observed  $B_y < 0$ , whereas C3 observed  $B_y > 0$ . On a few separate

332 occasions C1 did briefly observe  $B_y > 0$  (e.g. at 00:31:05 UT) but at these times C1 was

333 located above the neutral sheet ( $B_x > 0$ ), while C2 and C4 observed  $B_y < 0$  above the neutral

334 sheet. These variations in  $B_y$  imply the observation of a 'kink' in the field at the location of

335 C1, the ramifications of which are discussed further in section 4.2.

336

337 At times when  $B_x$  observed by C1 was negative, indicating that C1 was below the neutral

338 sheet, C1 generally observed negative (dawnward)  $v_{\perp y}$  (Fig. 3v) with a magnitude varying

339 between 100 and 200 km s<sup>-1</sup>. At times when  $B_x$  became positive, indicating that C1 was

340 above the neutral sheet, C1 observed positive (duskward)  $v_{\perp y}$  a majority of the time,

341 although this flow barely reached 100 km s<sup>-1</sup>. The negative enhancements in  $v_{\perp y}$  were

342 generally accompanied by negative enhancements in  $B_y$ . Across the interval, there was a

343 near continual  $v_x > 200$  km s<sup>-1</sup> flow (black dotted line in Fig. 3iv), peaking at almost 400 km

344 s<sup>-1</sup>, with concurrent peaks in the convective  $v_{\perp x}$  component (solid black line) of at least

345 200 km s<sup>-1</sup>. The convective flow measured by C3, however, was generally very weak ( $|v_{\perp}| <$

346 50 km s<sup>-1</sup>) throughout this period (solid green line in Fig 3iv).  $v_z$  (Fig. 3vi), as measured by

347 both C1 and C3 remained low in magnitude ( $< 100$  km s<sup>-1</sup>) for the duration of the interval,

348 with a few  $v_{\perp z}$  excursions above 100 km s<sup>-1</sup> observed by C1. The most significant

349 enhancements in  $v_{\perp z}$  seen by C1 appeared to occur in conjunction with the rapid current

350 sheet crossings between 00:30:50 and 00:32:00 UT. We discuss the implications of these

Formatted: Font: Italic

Formatted: Font: Italic, Subscript

351 observations in the context of the upstream IMF conditions and large-scale magnetospheric  
352 morphology in section 4.

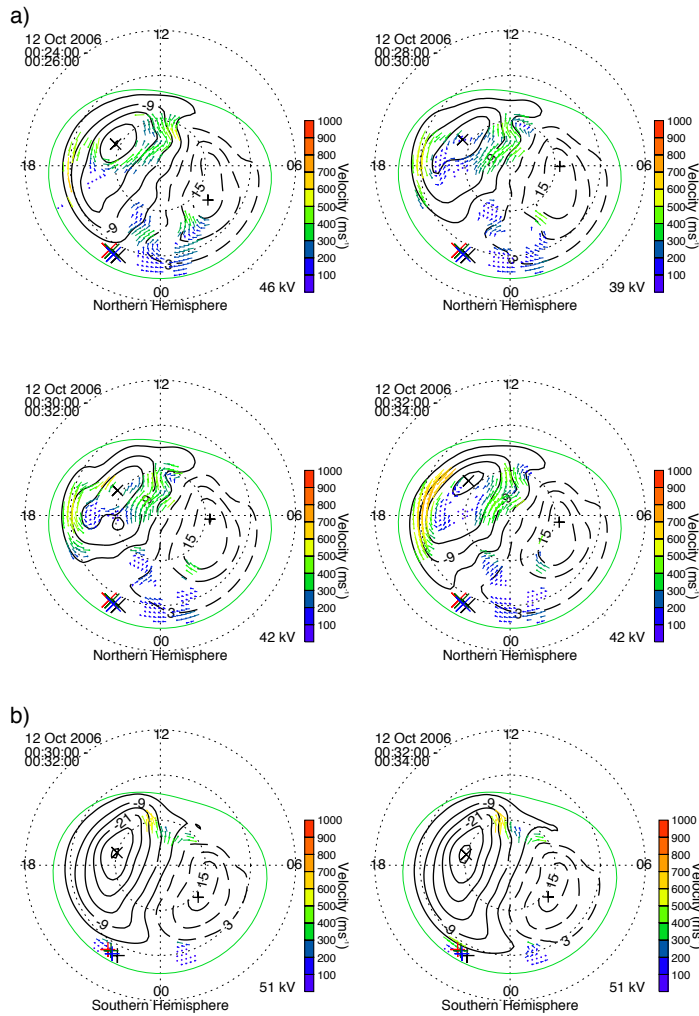
353

354

### 355 *3.3 Ionospheric Convection Observations*

356

357 To provide the large-scale context in which we can interpret the more localized  
358 observations from the Cluster spacecraft we show ionospheric convection observations in  
359 Figure 4. In Fig. 4a we present a series of four 2-minute integration SuperDARN maps of the  
360 northern hemisphere ionospheric convection pattern, beginning at 00:24 UT, and ending at  
361 00:34 UT, which encompasses our specific interval. In all maps, plasma is flowing anti-  
362 sunward across the polar cap at high latitudes, also with a strong duskward sense, with the  
363 direction of the convection reversing in the pre-midnight sector before returning sunward at  
364 lower latitudes.



365

366 **Figure 4:** Maps of the ionospheric plasma convection derived from SuperDARN

367 observations. Midnight is to the bottom of each map, noon to the top, dusk to the left and

368 dawn to the right. The dashed black circles are spaced every  $10^\circ$  in magnetic latitude. The

369 thicker solid and dashed black lines represent the plasma streamlines and are the contours

370 of the electrostatic potential. Flow vectors are plotted at the locations of radar observations

371 and these are color-coded based on the magnitude of their velocity. a) Four 2-minute

372 northern hemisphere maps from 00:24 – 00:26, 00:28 – 00:30, 00:30 – 00:32 and 00:32 –

373 00:34 UT, respectively. b) Two 2-minute southern hemisphere maps from 00:30 – 00:32 and  
374 00:32 – 00:34 UT, respectively. On each northern (southern) hemisphere map, the  
375 footpoints of the Cluster spacecraft constellation are shown by the X's (+s), mapped using  
376 the TA15 model.

377

378

379 Owing to the coupled nature of the magnetosphere-ionosphere system, the observed  
380 ionospheric convection pattern is indicative of the global-scale magnetospheric convection  
381 (Cowley, 1981). In this case, the typical symmetrical twin-cell convection pattern has been  
382 rotated clockwise, with the dawn cell extending across into the pre-midnight sector,  
383 indicative of convection that has been driven under the influence of a positive IMF  $B_y$   
384 component (e.g. Reistad et al., 2016, 2018). On each northern hemisphere map, the  
385 footpoints of the Cluster spacecraft constellation are indicated by the crosses (X), mapped  
386 using the TA15 model with the same parameterisation described in section 2.

387

388 Fig. 4b shows two 2-minute integration SuperDARN maps of the southern hemisphere  
389 ionospheric convection pattern, beginning at 00:30 UT, and ending at 00:34 UT. The  
390 associated footpoints of the Cluster spacecraft are indicated by the plus signs (+). Although  
391 the coverage of radar data is much less than in the northern hemisphere, there are data in  
392 the pre- and post-midnight sectors which appears to be influencing the location of the flow  
393 reversal region at the nightside end of the dusk cell. Opposite to the northern hemisphere  
394 case, it is the dusk cell in the south which is extending towards, or just beyond, the midnight  
395 meridian. This is also consistent with a large-scale positive IMF  $B_y$  influence, owing to the  
396 expected north-south asymmetry of the influence of IMF  $B_y$  in the magnetosphere (e.g.  
397 Pettigrew et al., 2010). The significance of these observations is further discussed in section  
398 4.1.

399

#### 400 **4. Analysis and Discussion**

401

402 We have presented observations of a dynamic interval of plasma flows and magnetic field in  
403 the Earth's magnetotail. In this section we discuss our rationale for interpreting the flows  
404 observed by C1 as being inconsistent with the large-scale convection expected based on the

405 ~~spacecraft location and magnetotail untwisting considerations, and our alternative~~

406 interpretation of their relationship to current sheet flapping.

407

#### 408 4.1 Evidence for an inconsistency with large-scale magnetotail untwisting

409 During the five-minute interval studied (00:28 – 00:33 UT) C1 measured a continually

410 fluctuating  $B_x$  component (Fig. 3i), indicative of multiple crossings of the tail current sheet.

411 C1 was the only spacecraft to measure this signature across the interval (although similar

412 signatures had been observed a few minutes earlier by C2 and C4). C1 also measured a

413 series of earthward convective magnetotail fast flows with varying dusk-dawn components.

414 The data in Fig. 3 i) and Fig. 3 v) illustrate that when  $B_x$  was positive (negative), a duskward

415 (dawnward)  $v_{\perp y}$  was generally observed. The observed dawnward flow in the southern

416 hemisphere, in particular, is inconsistent with the expected symmetric duskward flow at the

417 pre-midnight location of C1 which was, however, observed by C3. This suggests that the

418 typical ‘symmetrical’ Dungey-cycle return flow (e.g. Kissinger et al., 2012) cannot provide an

419 explanation for the flow observations made by C1. We thus turn our attention to other

420 possible explanations which we explore in detail, below.

421

422 The data in Fig. 3 ii) show that C1 tended to observe a negative  $B_y$  component. According to

423 the magnetotail untwisting hypothesis (e.g. Pitkänen et al., 2015), these flow and magnetic

424 field observations are consistent with a negative IMF  $B_y$  penetration. The IMF data

425 presented in Fig. 2a, on the other hand, revealed that IMF  $B_y$  was generally positive for

426 several hours prior to the fast flow interval (00:28 – 00:33 UT). Based on the IMF data alone,

427 therefore, one might expect that a positive IMF  $B_y$  will have penetrated into the

428 magnetosphere and thus ought to have determined the “expected” dusk-dawn direction of

429 the flow. In that case, the flows observed here would have a dusk-dawn sense that is not

430 explained by current theoretical models of magnetotail untwisting, meaning they are not

431 IMF  $B_y$ -controlled (e.g. Grocott et al., 2007). There are a number of possible explanations for

432 this discrepancy and we address each one in turn.

433

434 The first possibility is that our conclusion regarding the expected sense of IMF  $B_y$  control is

435 incorrect. As discussed above, the flows observed by Cluster would be consistent with the

436 magnetotail untwisting hypothesis in the case that we had IMF  $B_y < 0$  penetration. We

Deleted: and

Deleted: large-scale

Deleted: alternative

Deleted: Additionally, the

Deleted: -



442 noted in section 3.1 that there were three small negative IMF  $B_y$  excursions prior to our  
443 Cluster observations interval. Although the propagation of the IMF to the bow shock is  
444 accounted for in the OMNI data, there is uncertainty regarding the time it takes for the IMF  
445  $B_y$  to ‘propagate’ into the magnetotail. Uncertainties in IMF  $B_y$  propagation times (e.g. Case  
446 & Wild, 2012) have previously been cited as an explanation for observing an unexpected  
447 asymmetry (e.g. Pitkänen et al., 2013). Studies such as Tenfjord et al. (2015, 2017) and Case  
448 et al. (2018), for example, have suggested a reconfiguration time (to the prevailing IMF  $B_y$   
449 conditions) for nightside closed field lines of around 40 minutes. At ~00:28 UT (the  
450 beginning of our specific interval of interest), the IMF  $B_y$  had been positive for around  
451 50 minutes. Based on the Tenfjord timescale, this would thus imply that our interval was  
452 wholly IMF  $B_y > 0$  driven. Other studies, on the other hand, such as Browett et al. (2017),  
453 have shown that longer timescales of a few hours may be important.

454

455 However, for such long timescales to play a role one would expect to have observed a  
456 relatively persistent IMF  $B_y$  component during that time. The integrated IMF  $B_y$  over the  
457 hours prior to our interval was certainly convincingly  $B_y$ -positive, and it seems highly unlikely  
458 that a few minute-long fluctuations into the opposite IMF  $B_y$  polarity, 1 or 2 hours prior to  
459 the flows we observed, could have a significant influence. We can thus be confident that  
460 positive IMF  $B_y$  was governing the global magnetospheric dynamics in this case.

461

462 Despite this convincing argument that the IMF data alone imply a positive IMF  $B_y$   
463 penetration, we performed an additional analysis to further ensure that these negative  
464 excursions did not lead to a change in the global nature of the magnetosphere-ionosphere  
465 system. We inspected the concurrent northern hemisphere SuperDARN data (presented in  
466 Fig. 4a) to provide evidence of the large-scale convection pattern. If the large-scale flow is  
467 consistent with a positive IMF  $B_y$  component, then the magnetotail flows that we observed  
468 must be deviating from this for some reason and cannot be related to IMF  $B_y$  control. The  
469 SuperDARN data indeed confirm that the large-scale morphology of the system was  
470 consistent with a positive IMF  $B_y$  component (e.g. Lockwood 1993; Grocott et al., 2017;  
471 Reistad et al., 2018). This can be inferred from the general shape of the convection pattern,  
472 whereby across multiple maps (00:24 – 00:34 UT) the pattern was rotated clockwise, with  
473 the dawn cell having extended into the pre-midnight sector. That this is the expected

Deleted: -

475 convection pattern for an IMF  $B_y$ -driven magnetosphere is also supported by the concurrent  
476 low level of geomagnetic activity. The auroral AU and AL indices (not shown) confirm that  
477 this interval is geomagnetically quiet (AU and  $|AL|$  both less than (or of the order of) 10 nT),  
478 such that the nightside ionospheric convection asymmetry should be driven by IMF  $B_y$  rather  
479 than conductivity-driven features such as the Harang reversal which might otherwise  
480 complicate the auroral zone flows (e.g. Grocott et al., 2007; Grocott et al., 2008; Reistad et  
481 al., 2018).

482

483 The validity of the convection observations is further supported by the coverage of nightside  
484 data which were used to constrain the model convection pattern. The data used to create a  
485 SuperDARN convection map are supplemented by data from a statistical model (in this case  
486 Ruohoniemi & Greenwald, 1996) which is typically parameterised by the instantaneous IMF  
487 conditions. In the case that there is a lack of real data coverage, a created SuperDARN map  
488 will be strongly influenced by the model data, as opposed to real data, and thus would  
489 reflect a prediction of convection based on the IMF conditions. The maps shown in Fig. 4a  
490 illustrate that there were dozens of SuperDARN vectors in the midnight sector which were  
491 fitted to create the global convection maps. To confirm that these data were sufficient, and  
492 that the observed large-scale convection pattern was not being driven by model data, we  
493 parameterised the model in our analysis with IMF  $B_y = 0$ . Despite this, a clear IMF  $B_y$ -  
494 asymmetry exists, thus demonstrating that the observed large-scale IMF  $B_y > 0$  global  
495 convection patterns must be data-driven.

496

497 A second possible explanation for the discrepancy between the dusk-dawn direction of the  
498 local and global-scale convection concerns the certainty with which we can determine the  
499 location of the spacecraft with respect to the large-scale convection pattern. The untwisting  
500 hypothesis, as considered by e.g. Pitkänen et al. (2013, 2017), relies on the assumption that  
501 the convection cell to which the spacecraft is connected should be a factor of only  
502 hemisphere and the sense of IMF  $B_y$ . In other words, as discussed above, for IMF  $B_y > 0$ , the  
503 hypothesis dictates that C1 ought to be located on the dawn cell when above the neutral  
504 sheet and the dusk cell when below, at least in the case that the spacecraft is close to  
505 midnight (Grocott et al., 2007). This might be true statistically, but does not account for the  
506 dusk-dawn location of the spacecraft, which in this case was  $6 \lesssim Y_{GSM} \lesssim 7 R_E$ . If, as a result,

507 the spacecraft was actually located on the dusk cell when above the neutral sheet, and on  
508 the dawn cell when below the neutral sheet, then the sense of the observed plasma sheet  
509 flows would actually be consistent with the large-scale convection.

510

511 One way to specify which cell the spacecraft is located within is to map its location into the  
512 ionosphere. This has been done using TA15 and is shown by the crosses (X) on the northern  
513 hemisphere convection maps and by plus signs (+) on the southern hemisphere convection

514 maps, in Fig. 4a and 4b, respectively. Firstly, let us consider the northern hemisphere map  
515 from 00:24–00:26 UT in Fig. 4a: despite the lack of scatter in the immediate vicinity of the  
516 spacecraft footprints, it is noticeable how the spacecraft appear to map closer to the dusk  
517 cell than the dawn cell. For the remaining northern hemisphere maps, there is insufficient  
518 scatter to determine the exact division between the dusk and dawn convection cells, such  
519 that it is inconclusive as to which cell the Cluster spacecraft map to when above the neutral  
520 sheet. If Cluster did indeed map to the dusk convection cell, then the duskward flows in the

521 northern hemisphere plasma sheet, observed by C1 would actually be consistent with the  
522 large-scale convection pattern. Furthermore, given that the C2-C4 magnetic field  
523 observations are consistent with the local  $B_y$  being dominated by magnetotail flaring (as  
524 opposed to IMF  $B_y$ ) at the pre-midnight location of Cluster, it is likely that we would expect  
525 the return sense of the convection to be dominated here by the symmetric (duskward)  
526 element both above and below the neutral sheet (see e.g. Pitkänen et al., 2019).

527

528 If we instead consider the southern hemisphere maps in Fig. 4b we can be more certain of  
529 which cell the spacecraft map to. Owing to the IMF  $B_y$  positive nature of the convection (i.e.  
530 the more extended southern hemisphere dusk cell) and the pre-midnight location of the  
531 spacecraft, the footpoints are located quite convincingly on the dusk cell. This is despite the  
532 dusk-dawn asymmetry being less pronounced than that seen in the northern hemisphere  
533 (and the associated poorer coverage of southern hemisphere SuperDARN data). When  
534 below the neutral sheet C1 observed downward flows, meaning it would have to have been  
535 on the southern hemisphere dawn cell to be consistent with the large-scale convection,  
536 which is clearly not the case. Indeed, the observed downward flow in the southern  
537 hemisphere at this location could only be interpreted in terms of the untwisting hypothesis  
538 for a situation where we had clear IMF  $B_y < 0$  penetration (and associated extended dawn

Deleted: Consider first

Deleted: 30

Deleted: 32

Deleted: the spacecraft appear to map closer to the dawn cell than the dusk cell, such that the predominantly duskward flow that C1 observed in the northern hemisphere plasma sheet would seem to be inconsistent. However, it is worth considering that the pre-midnight location of the spacecraft, the proximity of the mapped footpoints to the dusk cell, and the level of uncertainty generally accepted to be present in field line mapping, may give credence to the possibility that the spacecraft actually mapped to the dusk cell in the northern hemisphere. If this was the case, then

Deleted: flows

Formatted: Font: Italic

Formatted: Font: Italic, Subscript

Formatted: Font: Italic

Formatted: Font: Italic, Subscript

Deleted: However, if

554 cell), which has already been ruled out. C3, meanwhile, continually observed duskward flow,  
 555 which appears to be consistent with the larger-scale convection. It seems much more likely,  
 556 therefore, that C1 observed flow that was associated with localized magnetic field dynamics  
 557 rather than being a signature of the large-scale convection.

558  
 559

560 *4.2 Evidence for a local perturbation in the magnetotail*

561 The lack of consistency with the large-scale convection leads us to a third explanation for  
 562 our observations, which is that there is a local perturbation within the tail that is  
 563 independent of any large-scale, IMF  $B_y$ -controlled asymmetry associated with magnetotail  
 564 untwisting. This is supported by the observations from the other Cluster spacecraft. The

565 low-level of flow seen by C3 is mostly duskward (Fig. 3v), ~~which would be consistent with~~  
 566 ~~untwisting for IMF  $B_y > 0$ , given its southern hemisphere location. We note, however, that~~  
 567 ~~due to the pre-midnight location of C3, one would also rightly expect to observe~~ duskward  
 568 flow ~~even in the case that there was no IMF  $B_y > 0$  control (e.g. Kissinger et al., 2012).~~

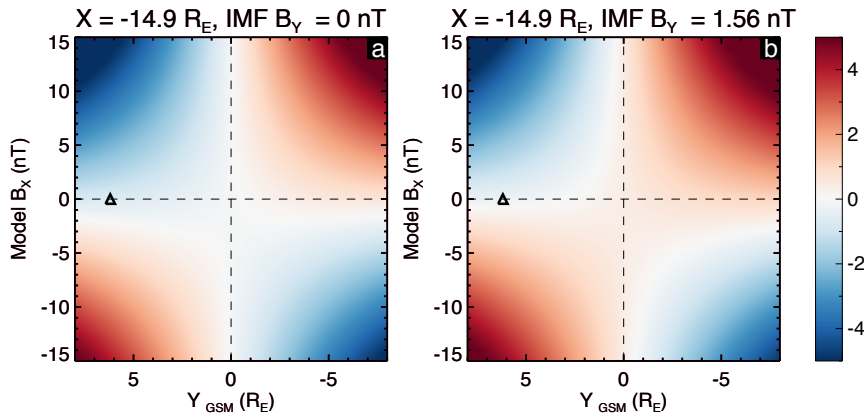
569 Further, in Fig. 2b v), up until the rapid  $B_x$  variations began at ~00:24 UT, fast duskward flow  
 570 in the southern hemisphere was also seen by C1. The fact that C3 continued to then observe  
 571 steady duskward flow, and no significant  $B_x$  change, suggests that the change in the nature  
 572 of the C1 observations after 00:24 UT must in-fact be due to some localized process that  
 573 was responsible for driving the dawnward component of the flows which was only observed  
 574 by C1.

575

576 This idea of a local perturbation is also supported by the variations in the local  $B_y$   
 577 component. Fig. 3 ii) illustrates the in-situ variations in  $B_y$  with time across the interval.  
 578 Despite there clearly being positive IMF  $B_y$  penetration globally (as confirmed by inspection  
 579 of the OMNI and SuperDARN data), C1, C2 and C4 all recorded mostly negative local  $B_y$   
 580 values. In the studies of, e.g., Pitkänen et al. (2013, 2017) this observation would have been  
 581 offered as evidence of a negative of IMF  $B_y$  penetration, thus supporting the untwisting  
 582 hypothesis. However, it is important to note that a negative local  $B_y$  component may be  
 583 wholly consistent with positive IMF  $B_y$ . There are, in fact, multiple sources of  $B_y$  in the tail,  
 584 such as magnetotail flaring (Fairfield, 1979), as well as tilt effects and current sheet warping  
 585 (see e.g. Petrukovich et al., 2005), in addition to a penetration of the IMF  $B_y$ . To fully

- Deleted: and therefore
- Deleted: the idea of
- Deleted: under
- Deleted: , given its southern hemisphere location
- Deleted: ; although, it should be noted that this observation would also be consistent with the
- Deleted: ed
- Deleted: absence of a large-scale asymmetry
- Deleted: no
- Formatted: Font: Italic
- Formatted: Font: Italic, Subscript
- Deleted: (e.g. Kissinger et al., 2012)

596 interpret the magnetic field observations, we must therefore consider the possible effects  
 597 of these phenomena on the presence of  $B_y$  in the tail at the specific location of each  
 598 spacecraft.



599  
 600

601 **Figure 5:** TA15 model magnetic field data. In each case, plotted is  $Y$  vs  $B_x$  [GSM], (at  
 602  $X = -14.9 R_E$ , i.e. the  $X$  position of C1 at  $\sim 00:28$  UT on 12 Oct 2006), with the TA15 modelled  
 603  $B_y$  value shown by the color bar on the right. The black triangle shows the  $Y$ -location of C1,  
 604 at  $B_x = 0$ . In panel (a) we have imposed IMF  $B_y = 0$ , and for panel (b) we have used the 1-  
 605 hour mean-averaged IMF  $B_y$  (+1.56 nT) in the hour prior to 00:28 UT.

606

607 To aid in this interpretation, we present TA15 model magnetic field data in Figure 5, to  
 608 provide an indication of the expected background  $B_y$ -component at the time of our interval.  
 609 These data, from  $X = -14.9 R_E$ , are plotted against  $Y$  [GSM]-position on the horizontal axis,  
 610 and against the  $B_x$ -component on the vertical axis. We have reversed the conventional  
 611 direction of the horizontal axis (negative to positive from left to right) to be consistent with  
 612 a view looking earthward from downtail. In panel (a) we show the field for the case that IMF  
 613  $B_y = 0$  and in panel (b) the case that IMF  $B_y = +1.56$  nT (the 1-hour mean-averaged IMF  $B_y$  in  
 614 the hour prior to 00:28 UT). The first conclusion we can make from consideration of the  $B_y$   
 615 component in Fig. 5a is how, even under no IMF  $B_y$  penetration, a 'background'  $B_y$  value will  
 616 exist in the tail purely dependent on location. In such a 'symmetric' tail, one would expect  
 617 the background  $B_y$  value to appear as one moves away from midnight toward the dusk-

618 dawn flanks, as well as further above and below the neutral sheet. Pre-midnight, we would  
619 expect to observe negative  $B_y$  above the neutral sheet ( $B_x > 0$ ), and positive  $B_y$  below the  
620 neutral sheet ( $B_x < 0$ ), with the opposite effect post-midnight. This is the well-known  
621 magnetotail flaring effect (Fairfield, 1979).

622

623 The data in Fig. 5a also show the effect of the negative (tailward) dipole tilt (as appropriate  
624 to our study interval) and current sheet warping on the local  $B_y$  component. According to  
625 Petrukovich (2011), the current sheet warping (controlled by the dipole tilt) is expected to  
626 add a negative  $B_y$  component pre-midnight and a positive  $B_y$  component post-midnight.  
627 Furthermore, the 'even tilt' effect is expected to add a negative  $B_y$  component to both the  
628 pre and post-midnight sectors for a negative tilt. This leads to the effect seen in Fig. 5a  
629 where in the pre-midnight sector, the location of the  $B_y$  polarity change occurs in the  
630 southern hemisphere (at  $B_x \approx -3$  nT).

631

632 Fig. 5b illustrates the scenario relevant to our case study, where we have additionally a  
633 global positive IMF  $B_y$  penetration. This additional positive  $B_y$  has the effect of moving the  
634 location of the pre-midnight  $B_y$  polarity change back up towards the neutral sheet. This  
635 explains why the Cluster spacecraft observed  $B_y \approx 0$  at times of  $B_x \approx 0$  during the few tens of  
636 minutes prior to our interval, as noted in section 3.2. This also explains why C2-3 and C4  
637 observed the polarity of  $B_y$  that they did throughout the interval. It is thus clear that positive  
638 IMF  $B_y$  penetration does not mean we should expect to observe positive  $B_y$  everywhere in  
639 the tail, rather, it simply means that there is expected to be some positive  $B_y$  perturbation  
640 to the already present 'background'  $B_y$  at a particular location. As Fig. 5b demonstrates, C2  
641 and C4 (located above the neutral sheet) are expected to have observed negative  $B_y$  even  
642 though positive IMF  $B_y$  has penetrated into the magnetotail, illustrating that the flaring  
643 effect is generally dominant at the spacecraft location. The background  $B_y$  expected at their  
644 location (pre-midnight,  $B_x > 0$ ), is negative and the IMF  $B_y$ -associated perturbation was not  
645 large enough to enforce a sign change in  $B_y$ .

646

647 The Cluster spacecraft in our study were all located pre-midnight (+Y GSM). From Figure 3,  
648 C2 and C4 observed positive  $B_x$ , and negative  $B_y$ , and at ~00:28 UT were located at around  
649  $Z = -1 R_E$  (Figure 1). C3, however, observed negative  $B_x$  and positive  $B_y$ , and was located at

Deleted:

651 around  $Z = -2.5 R_E$ . The location of the neutral sheet at  $\sim 00:28$  UT can therefore be said  
652 (locally) to have been somewhere between  $-1$  and  $-2.5 R_E$  in  $Z$ . C1 was located at around  $Z =$   
653  $-1.5 R_E$  and, throughout the five-minute interval, observed a  $B_x$  which continually fluctuated  
654 from positive to negative, yet observed mostly weakly negative  $B_y$ . For  $B_y$  to have remained  
655 negative, despite C1 moving above and below the neutral sheet, suggests that there was a  
656  $B_y$  negative 'kink' in the magnetotail that was localized to the vicinity of C1. This is further  
657 supported by the fact that numerous (albeit brief) positive  $B_y$  excursions occurred when C1  
658 was above the neutral sheet (as noted in section 3.2). We use the term 'kink' to highlight a  
659 deformation in the nearby field lines which results in the observed perturbations to the local  
660  $B_y$  component. We suggest that this deformation could be relatively small in terms of field  
661 line length, much like a kink in a cable or wire. In the following section, we investigate this  
662 kink in relation to the observed current sheet flapping.

663

664

#### 665 *4.3 Evidence for current sheet flapping as a source of the asymmetric flows*

666 If a localized magnetic field perturbation was associated with the lack of observation of the  
667 expected dusk-dawn flow for magnetotail untwisting, investigating its cause seems a  
668 worthwhile endeavour. The clear sinusoidal-like variation in  $B_x$  observed by C1, which is  
669 evidence of current sheet flapping (e.g. Runov et al., 2009), provides us with a starting point  
670 for this investigation. This flapping must be either highly localized or low in amplitude, as at  
671 the time of our five-minute flow interval (00:28 -00:33 UT), only C1 observed the flapping.  
672 MVA analysis (Sonnerup & Cahill, 1967) suggests that the flapping was a kink-like wave  
673 which was propagating downward (Rong et al., 2015; Wu et al., 2016), and therefore may  
674 have been a source of the observed dusk-dawn flow.

675

676 The causes of current sheet flapping have been discussed previously (Runov et al., 2009;  
677 Wei et al., 2019). One such cause has been attributed to localized, periodical reconnection –  
678 a process known to drive Bursty Bulk Flows (BBFs) in the magnetotail (Angelopoulos et al.,  
679 1994; Zhang et al., 2016). In fact, BBFs excited directly as a result of reconnection in the tail  
680 have been previously linked to magnetic fluctuations in the current sheet (Nakamura et al.,  
681 2009; Wu et al., 2016). Examining the data presented in Fig. 3 iii) and Fig. 3 iv), we note that  
682 C1 measured a generally positive  $B_z$ , with a few negative blips, as well as continually fast ( $v_x$

683 > 200 km s<sup>-1</sup>) earthward flow, peaking at over 370 km s<sup>-1</sup> with bursts of enhanced  
684 convective flow ( $v_{\perp x} > 200$  km s<sup>-1</sup>) also apparent. These observations are fairly consistent  
685 with (if slightly slower than) the original definition of a BBF (Angelopoulos et al., 1994). This,  
686 along with the absence of similar flow observations in the C3 data, suggests that C1 may  
687 have been located earthward of a localized reconnection site (owing to  $B_z > 0$ ), where  
688 persistent, localized reconnection was exciting fast earthward flow. The reconnection  
689 process may then have been driving the current sheet flapping, inducing the localized kink in  
690 the field, and ultimately controlling the dusk-dawn direction of the convective flow.

691

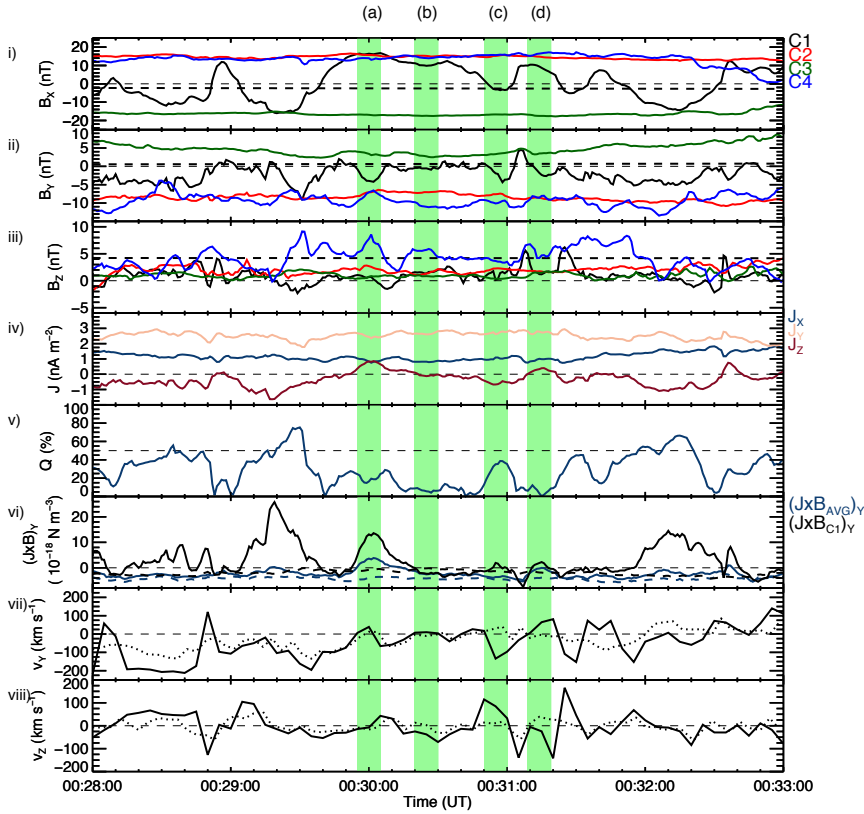
692

693 It is well known that the magnetic tension force is responsible for the acceleration of plasma  
694 following reconnection (Karlsson et al., 2015). Our observations of a dusk-dawn flow  
695 component may be related to the localized magnetic tension forces driving and directing  
696 plasma flows in association with the flapping. In order to provide some scope to this  
697 suggestion, we attempted to find the direction of the  $\mathbf{J} \times \mathbf{B}$  forces acting on the plasma. We  
698 used the curlometer technique (Dunlop et al., 1988, 2002), to estimate the average current  
699 density,  $\mathbf{J}$ , flowing through the volume bound by the spacecraft tetrahedron. The  $\mathbf{J} \times \mathbf{B}$   
700 force density [N m<sup>-3</sup>] is then calculated, firstly, by taking the cross product of  $\mathbf{J}$  with the  
701 average magnetic field vector  $\mathbf{B}$  from the four-spacecraft ( $\mathbf{B}_{AVG}$ ). We also calculate  $\mathbf{J} \times \mathbf{B}$   
702 using solely  $\mathbf{B}$  from C1 ( $\mathbf{B}_{C1}$ ), in order to provide a more local estimate for  $\mathbf{J} \times \mathbf{B}$  at the  
703 location of C1.

704

705 In order to check the validity of using the curlometer approach, we calculated the quality  
706 parameter,  $Q$ , defined as  $|\nabla \cdot \mathbf{B}|/|\nabla \times \mathbf{B}|$ . It is generally accepted that a value of  $Q < 0.5$  is  
707 required for a current estimate to be valid. Hence, the value of  $Q$ , along with due  
708 consideration of the spacecraft configuration and its orientation relative to the magnetic  
709 field structure, may be used as a monitor of how reliable the curlometer approach is  
710 (Dunlop et al., 2002). This is discussed further below, in reference to the analysis shown in  
711 Figure 6.





712  
 713 **Figure 6:** i-iii) The local magnetic field vector  $\mathbf{B}$  ( $B_x$ ,  $B_y$ ,  $B_z$ ) observed by C1-4, as shown  
 714 previously (solid lines) and the TA15 modelled  $\mathbf{B}$  vector for C1 (dashed black lines). iv) The  
 715 components of the current density vector  $\mathbf{J}$  ( $J_x$ ,  $J_y$ ,  $J_z$ ), v)  $Q$ , vi)  $(\mathbf{J} \times \mathbf{B}_{AVG})_y$  (solid blue line)  
 716 and  $(\mathbf{J} \times \mathbf{B}_{C1})_y$  (solid black line). The dashed blue and black lines indicate the equivalent  
 717 calculation where the TA15 model  $\mathbf{B}$  field of C1 has been used (see text). vii)  $v_y$  ( $v_{\perp y}$  in solid  
 718 lines), observed by C1 and viii)  $v_z$  ( $v_{\perp z}$  in solid lines), also observed by C1. The green  
 719 highlighted regions labelled (a), (b), (c) and (d) correspond to four specific time-windows of  
 720 interest (discussed in-text).

721  
 722 Shown in Fig. 6 i-iii) are the local magnetic field  $B_x$ ,  $B_y$  and  $B_z$  components, as presented  
 723 previously. In Fig. 6 iv) are the current density  $J_x$ ,  $J_y$  and  $J_z$  components determined from the

724 curlometer analysis. In Fig. 6 vi) is the dusk-dawn component of  $\mathbf{J} \times \mathbf{B}_{AVG}$  and  $\mathbf{J} \times \mathbf{B}_{C1}$ .  
 725 Finally, in Fig. 6 vii) and viii) are the dusk-dawn and north-south components of the flow  
 726 (and field-perpendicular flow) observed by C1, as shown previously. In panels (i-iii), the  
 727 dashed black line represents the TA15 modelled magnetic field (see section 4.2) at the  
 728 location of C1. In panel (vi) the dashed blue and black lines represent the  $(\mathbf{J} \times \mathbf{B}_{AVG})_y$  and  $(\mathbf{J}$   
 729  $\times \mathbf{B}_{C1})_y$  forces, respectively, where  $\mathbf{J}$  and  $\mathbf{J} \times \mathbf{B}$  have been computed using the model field  
 730 at the location of C1 and the true magnetic fields measured by C2-C4. These ‘model  $(\mathbf{J} \times \mathbf{B})_y$   
 731 forces’ have been computed to provide an illustration of what one would expect the  
 732 ‘unperturbed’ magnetic field of C1 and the associated  $(\mathbf{J} \times \mathbf{B})_y$  force to look like, in the  
 733 absence of any dynamical effects such as current sheet flapping or field line ‘kinking’. In  
 734 both cases, the model  $(\mathbf{J} \times \mathbf{B})_y$  forces are weakly downward, consistent with the  
 735 ‘background curvature’ of the magnetic field at this pre-midnight location (see Fig. 7). Fig. 6  
 736 v) suggests that our curlometer approach is generally appropriate, as  $Q$  mostly remains  
 737 below 50% (horizontal dashed line) for the five-minute interval. We note that, unlike in  
 738 previous studies which have used the curlometer technique at inter-spacecraft separation  
 739 distances of  $\ll 1 R_E$  (e.g. Dunlop et al., 2002; Runov et al., 2003), in our case the Cluster  
 740 spacecraft separation is large ( $\gtrsim 1 R_E$ ). Therefore, the curlometer is likely to be an  
 741 underestimate of the true current at these scale sizes. Critically, however, the spacecraft  
 742 configuration is such that the estimate of the direction of the currents should be stable.  
 743 Thus, although the volume enclosed by the spacecraft is greater than the scale sizes of the  
 744 current sheet flapping and kink, a reliable estimate of the direction of the net  $\mathbf{J} \times \mathbf{B}$  force  
 745 within the enclosed volume may still be obtained.

746

747 Two key features of Figure 6 are apparent. Firstly, it appears as though the perturbations to  
 748  $(\mathbf{J} \times \mathbf{B})_y$  are mostly associated with the magnetic field perturbations generally only observed  
 749 by C1. This is made apparent by comparing  $(\mathbf{J} \times \mathbf{B}_{C1})_y$  with  $(\mathbf{J} \times \mathbf{B}_{AVG})_y$ , where the  
 750 perturbations are much larger in magnitude for  $(\mathbf{J} \times \mathbf{B}_{C1})_y$ . We also note that both  
 751  $(\mathbf{J} \times \mathbf{B}_{AVG})_y$  and  $(\mathbf{J} \times \mathbf{B}_{C1})_y$  are effectively always positive with respect to their model  
 752 equivalents. However,  $(\mathbf{J} \times \mathbf{B}_{AVG})_y$  is still mostly net negative whereas  $(\mathbf{J} \times \mathbf{B}_{C1})_y$  is net  
 753 positive. This suggests that using  $\mathbf{B}_{C1}$ , rather than  $\mathbf{B}_{AVG}$  in calculating  $(\mathbf{J} \times \mathbf{B})_y$  has overall

754 reduced the effects of the larger-scale background field curvature (incorporated by  
755 including the other spacecraft). Second, the magnetic field and flow dynamics evident in Fig.  
756 6 appear to almost always be associated with positive (duskward) enhancements in  $(\mathbf{J} \times \mathbf{B})_y$ ,  
757 in contrast to the model dawnward sense of  $(\mathbf{J} \times \mathbf{B})_y$ . This is particularly evident in the case  
758 of  $(\mathbf{J} \times \mathbf{B}_{C1})_y$ , but also generally true in the case of  $(\mathbf{J} \times \mathbf{B}_{AVG})_y$ . We therefore suggest that  
759 the dynamic behaviour of  $(\mathbf{J} \times \mathbf{B})_y$  is simply consistent with the localized kinks and flapping  
760 in the magnetic field that are associated with the transient perturbations to the dusk-dawn  
761 flow observed by C1.

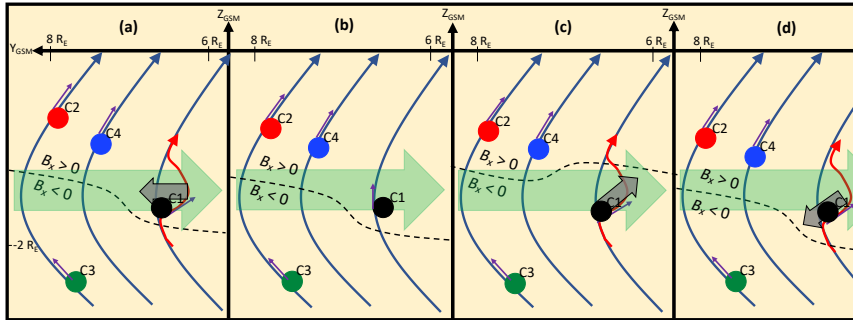
762

763

#### 764 4.4 Visualization of the observed dynamics

765 In an effort to visualize these plasma sheet dynamics, we show in Figure 7 a series of  
766 sketches that attempt to associate the observed magnetic field perturbations with the  
767 observed dusk-dawn convective flows. The panels correspond to the four time-windows  
768 indicated on Figure 6 by the highlighted regions labelled a-d. In each panel, we indicate the  
769 approximate relative position of the 4 Cluster spacecraft in GSM coordinates, and the  
770 appropriate sense of  $B_y$  measured by each spacecraft is shown by the purple arrows at each  
771 spacecraft location (the Z-component of the field was in fact generally small, and has been  
772 exaggerated here for illustrative purposes). We also superimpose nominal plasma sheet  
773 field lines (again with an exaggerated extent in Z) that display the sense of  $B_y$  implied by the  
774 TA15 data presented in Figure 5 (long blue curved arrows). The dashed lines represent the  
775 location of the neutral sheet at the end of each time window. This is tilted slightly, as  
776 appropriate for IMF  $B_y > 0$ , but with the end-state of the “flap” of the current sheet implied  
777 by the sign of  $B_x$  observed by C1. In red is the perturbation to the field implied by the sign of  
778  $B_y$  observed by C1.

779



780

781

782 **Figure 7:** Schematic diagrams of the observed magnetic field perturbations and dusk-dawn  
 783 convective flows during the time-windows indicated in Fig. 6 by the highlighted regions. The  
 784 approximate locations of the four Cluster spacecraft relative to one-another in the Y-Z GSM  
 785 plane are indicated (not to scale) by the colored circles. The curved blue arrows represent  
 786 magnetic field lines, and the short purple arrow indicates the local sense of  $B_y$  at the  
 787 location of each spacecraft. The dashed black line indicates the current sheet. In panels (a),  
 788 (c) and (d), the curved red arrow shows the 'kinked' magnetic field line. The long thick green  
 789 arrow shows the direction of the model  $(\mathbf{J} \times \mathbf{B})_y$  force associated with the background  
 790 curvature of the magnetic field, and the small thick gray arrow shows the direction of the  
 791 dusk-dawn convective flow observed by C1.

792

793

794 In Fig. 7a C1 is located above the current sheet and measured negative  $B_y$ . A weakly  
 795 duskward convective flow was observed at this time (as indicated by the thick gray arrow),  
 796 consistent with the duskward sense of the  $(\mathbf{J} \times \mathbf{B})_y$  force, and opposite to the sense of the  
 797 model  $(\mathbf{J} \times \mathbf{B})_y$  force associated with the background curvature of the magnetic field. In Fig.  
 798 7b, C1 is still above the current sheet but measured  $B_y \approx 0$  and no dusk-dawn convective  
 799 flow. In Fig. 7c C1 is shown below the current sheet, where the background  $B_y$  would be  
 800 positive (see Fig. 5b). C1 instead observed an increasingly negative  $B_y$ , which we suggest is  
 801 associated with the presence of the kink in the field. At the same time, C1 also observed a  
 802 convective plasma flow with downward and slightly upward (+Z) component (thick gray

803 arrow). We therefore suggest that the flow was associated with the upward/dawnward flap  
 804 of the current sheet, and that the dawnward sense of the flow likely also resulted in the  
 805 increase in negative  $B_y$  seen during the time-window shown in Fig. 6c. The positive  
 806  $(\mathbf{J} \times \mathbf{B}_{C1})_y$  at this time, whilst inconsistent with the dawnward sense of the flow, is therefore  
 807 consistent with the curvature of the magnetic field associated with the kink.  $(\mathbf{J} \times \mathbf{B}_{AVG})_y$ ,  
 808 meanwhile, was negative, likely due to incorporating the larger-scale background curvature  
 809 of the magnetic field observed by the other spacecraft. In Fig. 7d C1 is shown above the  
 810 current sheet, where it observed a weakly negative  $B_y$ . In this case, C1 observed a  
 811 convective plasma flow with duskward and slightly downward ( $-Z$ ) component. Similarly to  
 812 in Fig. 7a, this flow occurred in concert with a positive enhancement in  $(\mathbf{J} \times \mathbf{B})_y$  relative to  
 813 the model  $(\mathbf{J} \times \mathbf{B})_y$ . This flow would therefore seem to be associated with the downward  
 814 flap of the current sheet, and its duskward sense could indicate that it is acting to reduce  
 815 the negative kink in  $B_y$  that is apparent over the time-window shown in Fig. 6d.

816  
 817 Whilst we acknowledge a degree of uncertainty in the details of the interpretation  
 818 presented above of the specific relationship between the flows and the field, it serves to  
 819 illustrate three observations about this interval of which we can be very certain: 1) The IMF,  
 820 ionospheric convection, and comparison of the plasma sheet magnetic field observations to  
 821 the TA15 model field, all lead to the expectation of an IMF  $B_y > 0$  large-scale asymmetry in  
 822 the magnetosphere. 2) The Cluster 1 spacecraft observed convective flow with a dusk-dawn  
 823 component that was inconsistent with current theories of IMF  $B_y$ -induced dusk-dawn flows  
 824 associated with magnetotail untwisting. Notably, the observed downward flow in the  
 825 southern hemisphere, whilst inconsistent with IMF  $B_y > 0$ , was also inconsistent with the  
 826 expected (symmetric) duskward flow at this pre-midnight location even in the absence of  
 827 IMF  $B_y$  control. 3) Magnetic field perturbations that were indicative of a localized current  
 828 sheet flapping and dusk-dawn kink in the field occurred coincident with the flows. It  
 829 therefore seems likely that in this case the IMF  $B_y$ -driven asymmetry, or indeed the  
 830 symmetric flow expected at the spacecraft location, was being overridden by the localized  
 831 dynamics in governing the dusk-dawn component of the flow.

832

833

Formatted: Font: Italic

Formatted: Font: Italic, Subscript

Formatted: Font: Italic, Subscript

Deleted: We therefore note that the observations presented here cannot be attributed to the current model of large-scale magnetotail untwisting.

Formatted: Font: Italic

Deleted: being overridden by

Deleted: ¶  
¶

840 **5. Summary**

841

842 We have presented a case study from 12 October 2006 revealing a dynamic interval of  
843 plasma flows and current sheet flapping, observed by the Cluster 1 spacecraft. The key  
844 observations presented in this study may be summarised as follows:

845

846 • The OMNI data revealed that the IMF  $B_y$  had been positive for several hours prior to  
847 our interval of Cluster data, with the exception of three short-lived negative  
848 excursions.

849 • The SuperDARN ionospheric convection observations revealed a large-scale  
850 asymmetry consistent with IMF  $B_y > 0$ , confirming the absence of a large-scale  
851 asymmetry in the flow pattern that might explain the downward flows observed by  
852 C1.

853 • C1 observed a changing  $B_x$  magnetic field component and associated duskward ( $v_{\perp y}$   
854  $> 0$ ) flow when in the northern magnetic hemisphere, and dawnward ( $v_{\perp y} < 0$ ) flow  
855 in the southern magnetic hemisphere.

856 • The C2, C3 and C4 magnetic field observations suggested that the local  $B_y$  was being  
857 dominated by magnetotail flaring, as opposed to IMF  $B_y$ . C3 also observed duskward  
858 flow in the southern magnetic hemisphere, consistent with the symmetric flow  
859 expected owing to the pre-midnight location of the spacecraft.

860

861 Contrary to the results of a number of previous studies in the literature, during this  
862 particular interval, the dusk-dawn sense of the convective magnetotail flows ( $v_{\perp y}$ ); and in  
863 particular, the dawnward flow observed in the southern hemisphere, does not agree with  
864 expectations based on the theoretical understanding of global magnetotail untwisting and  
865 the prevailing positive IMF  $B_y$  conditions, nor to expectations based on the location of the  
866 spacecraft and associated magnetotail flaring. We instead attribute the flows to a localized  
867 magnetic field perturbation, or 'kink' in the magnetotail, which appears to have been  
868 independent of any large-scale dynamics and may have instead been related to the  
869 observed current sheet flapping. We attributed the current sheet flapping to being driven  
870 by localized reconnection, itself inferred from the presence of the observed bursty fast

**Deleted:** , confirming the absence of a large-scale asymmetry in the flow pattern that might explain the downward flows observed by C1.

**Formatted:** Font: Italic

**Formatted:** Font: Italic, Subscript

874 earthward flow ( $v_{\perp x} \approx 200 \text{ km s}^{-1}$ ). Analysis using the curlometer technique suggests that  
875 the  $(\mathbf{J} \times \mathbf{B})_y$  force is consistent with the localized kinks and flapping in the magnetic field  
876 that are associated with the transient perturbations to the dusk-dawn flow observed by C1.

877  
878

879 Although evidence for the large-scale penetration of IMF  $B_y > 0$  is apparent, the IMF  $B_y > 0$   
880 penetration at the location of C1 appears to have been unable to override the variable dusk-  
881 dawn flow associated with the current sheet flapping. Further studies by the authors are  
882 currently underway to determine if such flows are a frequent occurrence, and to consider,  
883 and account for, localized tail dynamics more fully in a statistical analysis of the magnetotail  
884 flows.

885

#### 886 **Acknowledgements**

887

888 The authors would like to thank the FGM and CIS teams as part of the Cluster mission and  
889 acknowledge the Cluster Science Archive (Laakso et al., 2010) as the source of the Cluster  
890 data. We also wish to thank the OMNIWeb as the source of the solar wind and IMF data.  
891 The authors acknowledge the use of SuperDARN data. SuperDARN is a collection of radars  
892 funded by national scientific funding agencies of Australia, Canada, China, France, Italy,  
893 Japan, Norway, South Africa, United Kingdom, and United States of America, and we thank  
894 the international PI team for providing the data. The authors acknowledge access to the  
895 SuperDARN database via BAS data mirror (<http://bslsuperdarn.ncerc-bas.ac.uk:8093/docs/>)  
896 and are grateful for use of the Radar Software Toolkit (RST v4.2  
897 <https://zenodo.org/record/1403226#.Xy0u7y3MxTY>) with which the raw radar data were  
898 processed. We acknowledge the WDC for Geomagnetism, Kyoto, for use of the auroral  
899 electrojet indices, which may be obtained from <http://wdc.kugi.kyoto-u.ac.jp/aedir/>. We are  
900 also grateful to Haje Korth for providing the IDL Geopack DLM containing the Tsyganenko  
901 magnetic field model routines and coordinate system conversions and wish to thank Nikolai  
902 Tsyganenko for useful discussion of his magnetic field models. Finally, we are thankful for  
903 the advice of Malcolm Dunlop regarding the applicability of the curlometer technique at  
904 large spacecraft separations. This research was undertaken with the support of funding  
905 from the following sources: Lancaster University Faculty of Science and Technology  
906 studentship (JHL), STFC Consolidated grant no. ST/R000816/1 (NAC, AG), NERC standard  
907 grant nos. NE/P001556/1 and NE/T000937/1 (MTW, AG).

908

#### 909 **References**

910

911 Angelopoulos, V., Baumjohann, W., Kennel, C. F., Coroniti, F. V., Kivelson, M. G., Pellat, R.,  
912 Walker, R. J., Lühr, H. and Paschmann, G. (1992). Bursty bulk flows in the inner central  
913 plasma sheet. *J. Geophys. Res.*, *97* (A4), 4027-4039. doi:10.1029/91JA02701

914

- 915 Angelopoulos, V., Kennel, C. F., Coroniti, F. V., Pellat, R., Kivelson, M. G., Walker, R. J.,  
916 Russell, C. T., Baumjohann, W., Feldman W. C. and Gosling, J. T. (1994). Statistical  
917 characteristics of bursty bulk flow events. *J. Geophys. Res.*, *99* (A11), 21,257-21,280.  
918 doi:10.1029/94JA01263  
919
- 920 Balogh, A., Carr, C. M., Acuña, M. H., Dunlop, M. W., Beek, T. J., Brown, P., Fornacon, K. -H.,  
921 Georgescu, E., Glassmeier, K. -H., Harris, J., Musmann, G., Oddy, T. and Scwingenschuh, K.  
922 (2001). The Cluster magnetic field investigation: Overview of in-flight performance and  
923 initial results. *Ann. Geophys.*, *19*, 1207-1217. doi: 10.5194/angeo-19-1207-2001  
924
- 925 Baumjohann, W., Paschmann, G. and Cattell, C. A. (1989). Average Properties in the Central  
926 Plasma Sheet. *Journal of Geophysical Research*, *94* (A6), 6597-6606. doi:  
927 10.1029/JA094iA06p06597  
928
- 929 Browett, S. D., Fear, R. C., Grocott, A., and Milan, S. E. (2017). Timescales for the penetration  
930 of IMF  $B_y$  into the Earth's magnetotail. *J. Geophys. Res.: Space Physics*, *122* (1), 579-593.  
931 doi:10.1002/2016JA023198  
932
- 933 Cao, J. B., Ma, Y. D., Parks, G., Rème, H., Dandouras, I., Nakamura, R., Zhang, T. L., Zong, Q.,  
934 Lucek, E., Carr, C. M., Liu, Z. X. and Zhou, G. C. (2006). Joint observations by Cluster satellites  
935 of bursty bulk flows in the magnetotail. *J. Geophys. Res.*, *111* (A4), A04206.  
936 doi:10.1029/2005JA011322  
937
- 938 Case, N. A., Grocott, A., Haaland, S., Martin, C. J., and Nagai, T. (2018). Response of the  
939 Earth's Neutral Sheet to Reversals in the IMF  $B_y$  component. *J. Geophys. Res.*, *123* (10),  
940 8206-8218. doi:10.1029/2018JA025712  
941
- 942 Case, N. A. and Wild, J. (2012). A statistical comparison of solar wind propagation delays  
943 derived from multispacecraft techniques. *J. Geophys Res.*, *117* (A2), A02101,  
944 doi:10.1029/2011JA016946.  
945
- 946 Chisham G., Lester, M., Milan, S. E., Freeman, M. P., Bristow, W. A., Grocott A., McWilliams,  
947 K. A., Ruohoniemi, J. M., Yeoman, T. K., Dyson, P. L., Greenwald, R. A., Kikuchi, T., Pinnock,  
948 M., Rash, J. P. S., Sato, N., Sofko, G. J., Villain, J. -P. and Walker, A. D. M. et al. (2007). A  
949 decade of the Super Dual Auroral Radar Network (SuperDARN): scientific achievements,  
950 new techniques and future directions. *Surveys in Geophysics* *28*, 33-109.  
951 doi:10.1007/s10712-007-9017-8  
952
- 953 Cowley, S. W. H. (1981). Magnetospheric asymmetries associated with the y-component of  
954 the IMF. *Planet Space Sci*, *29* (1), 79-96. doi:10.1016/0032-0633(81)90141-0  
955
- 956 Dungey, J. W. (1961). Interplanetary magnetic field and the auroral zones. *Phys. Rev. Lett.*, *6*,  
957 47-48. doi:10.1103/PhysRevLett.6.47  
958
- 959 Dunlop, M. W., Southwood, D. J., Glassmeier, K. -H., and Neubauer, F. M. (1988). Analysis of  
960 multipoint magnetometer data. *Advances in Space Research*, *8* (9-10), 273-277.  
961 doi:10.1016/0273-1177(88)90141-X



- 962  
963 Dunlop, M. W., Balogh, A., Glassmeier, K. -H. and Robert, P. (2002). Four-point Cluster  
964 application of magnetic field analysis tools: The Curlometer. *J. Geophys. Res.*, *107* (A11).  
965 doi:10.1029/2001JA005088  
966  
967 Escoubet, C. P., Fehringer, M. and Goldstein, M. (2001). The Cluster Mission. *Ann. Geophys.*,  
968 *19*, 1197 – 1200. doi:10.5194/angeo-19-1197-2001  
969  
970 Fairfield, D. H. (1979). On the Average Configuration Of The Geomagnetic Tail. *J. Geophys.*  
971 *Res.*, *84* (A5), 1950-1958. doi:10.1029/JA084iA05p01950  
972  
973 Frühauff, D. and Glassmeier, K.-H. (2016). Statistical analysis of magnetotail fast flows and  
974 related magnetic disturbances. *Ann. Geophys.*, *34*, 399-409. doi:10.5194/angeo-34-399-  
975 2016  
976  
977 Grocott, A. (2017). Time Dependence of Dawn-Dusk Asymmetries in the Terrestrial  
978 Ionospheric Convection Pattern. In: Haaland, S. et al. (2017), *Dawn-Dusk Asymmetries in*  
979 *Planetary Plasma Environments*, John Wiley and Sons, Inc., 107-123  
980  
981 Grocott, A., Yeoman, T. K., Nakamura, R., Cowley, S. W. H, Frey, H. U., Rème, H. and Klecker,  
982 B. J. (2004a). Multi-instrument observations of the ionospheric counterpart of a bursty bulk  
983 flow in the near-Earth plasma sheet. *Ann. Geophys.*, *22*, 1061-1075, 1432-0576/ag/2004-22-  
984 1061.  
985  
986 Grocott, A., Yeoman, T. K., Cowley, S. W. H, and Rème, H. (2004b). Multi-instrument  
987 observations of bursty bulk flows and their ionospheric counterparts. *Proc. Seventh Internat.*  
988 *Conf. on Substorms*, UDK-52-854, FMI, Helsinki, Finland, 107-110.  
989  
990 Grocott, A., Badman, S. V., Cowley, S. W. H, and Cripps (2004c). The influence of the IMF  $B_y$   
991 on the nature of the nightside high-latitude ionospheric flow during intervals of positive IMF  
992  $B_z$ . *Ann. Geophys.*, *22*, 1755-1764, doi:10.5194/angeo-22-1755-2004.  
993  
994 Grocott, A., Yeoman, T. K., Milan, S. E. and Cowley, S. W. H. (2005), Interhemispheric  
995 observations of the ionospheric signature of tail reconnection during IMF-northward non-  
996 substorm intervals, *Ann. Geophys.*, *23*, 1763–1770. doi:10.5194/angeo-23-1763-2005.  
997  
998 Grocott, A., Yeoman, T. K., Milan, S. E., Amm, O., Frey, H. U., Juusola, L., Nakamura, R.,  
999 Owen, C. J., Rème, H. and Takada, T. (2007). Multi-scale observations of magnetotail flux  
1000 transport during IMF-northward non-substorm intervals. *Ann. Geophys.*, *25*, 1709-1720.  
1001 doi:10.5194/angeo-25-1709-2007  
1002  
1003 Grocott, A., Milan, S. E. and Yeoman, T. K. (2008). Interplanetary magnetic field control of  
1004 fast azimuthal flows in the nightside high-latitude ionosphere, *Geophys. Res. Lett.*, *35*,  
1005 L08102, doi:10.1029/2008GL033545.  
1006

- 1007 Haaland, S., Runov, A. and Forsyth, C. (2017). Dawn-Dusk Asymmetries in Planetary Plasma  
1008 Environments, *Geophysical Monograph 230, First Edition. American Geophysical Union.*  
1009 Published 2017 by John Wiley & Sons, Inc.  
1010
- 1011 Karlsson, T., Hamrin, M., Nilsson, H., Kullen, A., and Pitkänen, T. (2015). Magnetic forces  
1012 associated with bursty bulk flows in the Earth's magnetotail. *Geophys. Res. Lett.*, *42* (9),  
1013 3122-3128. doi:10.1002/2015GL063999  
1014
- 1015 Kiehas, S. A., Runov, A., Angelopoulos, V., Hietala, H. and Korovinskiy, D. (2018). Magnetotail  
1016 Fast Flow Occurrence Rate and Dawn-Dusk Asymmetry at  $X_{GSM} \sim -60 R_E$ . *J. Geophys. Res.:  
1017 Space Physics*, *123* (3), 1767 – 1778. doi:10.1002/2017JA024776  
1018
- 1019 King, J. H., and Papitashvili, N. E. (2005). Solar wind spatial scales in and comparisons of  
1020 hourly Wind and ACE plasma and magnetic field data. *J. Geophys. Res.*, *110*, A02104.  
1021 doi:10.1029/2004JA010649  
1022
- 1023 Kissinger, J., McPherron, R. L., Hsu, T. -S. and Angelopoulos, V. (2012). Diversion of plasma  
1024 due to high pressure in the inner magnetosphere during steady magnetospheric convection.  
1025 *J. Geophys. Res.*, *117*, A05206. doi:10.1029/2012JA017579  
1026
- 1027 Khurana, K. K., Walker, R. J., and Ogino, T. (1996). Magnetospheric convection in the  
1028 presence of interplanetary magnetic field By: A conceptual model and simulations. *J.  
1029 Geophys. Res.*, *101* (A3), 4907–4916. doi:10.1029/95JA03673  
1030
- 1031 Kubyshkina, D. I., Sormakov, D. A., Sergeev, V. A., Semenov, V. S., Erkaev, N. V., Kubyshkin, I.  
1032 V., Ganushkina, N. Yu. And Dubyagin, S. V. (2014). How to distinguish between kink and  
1033 sausage modes in flapping oscillations? *J. Geophys. Res.*, *119*, 3,002-3,015.  
1034 doi:10.1002/2013JA019477.  
1035
- 1036 Laakso, H., C. Perry, S. McCaffrey, D. Herment, A.J. Allen, C.C. Harvey, C.P. Escoubet, C.  
1037 Gruenberger, M.G.G.T. Taylor, and R. Turner (2010), Cluster Active Archive: Overview, 3-37,  
1038 The Cluster Active Archive, Astrophysics and Space Science Proceedings, H. Laakso et al.  
1039 (eds.), Springer.  
1040
- 1041 Lockwood, M. (1993), Modelling high-latitude ionosphere for time-varying plasma  
1042 convection. IEE Proceedings-H, Vol. 140. No. 2. doi:10.1049/ip-h-2.1993.0015  
1043
- 1044 Malova, H. V., Zelenyi, L. M., Popov, V. Y., Petrukovich, A. A. and Runov, A. V. (2007).  
1045 Asymmetric thin current sheets in the Earth's magnetotail. *Geophys. Res. Lett.*, *34* (16),  
1046 L16108. doi:10.1029/2007GL030011  
1047
- 1048 McPherron, R. L., Hsu, T. -S., Kissinger, J., Chu, X., and Angelopoulos, V., (2011).  
1049 Characteristics of plasma flows at the inner edge of the plasma sheet. *J. Geophys. Res.*, *116*  
1050 (A5), A00133. doi:10.1029/2010JA015923  
1051
- 1052 Nakamura, R., Baumjohann, W., Klecker, B., Bogdanova, Y., Balogh, A., Rème, H., Bosqued, J.  
1053 M., Dandouras, I., Sauvaud, J. A., Glassmeier, K. -H., Kistler, L., Mouikis, C., Zhang, T. L.,

- 1054 Eichelberger, H. and Runov, A. (2002). Motion of the dipolarization front during a flow burst  
1055 event observed by Cluster. *Geophys. Res. Lett.*, 29 (20), 1942. doi:10.1029/2002GL015763  
1056
- 1057 Nakamura, R., Retinò, A., Baumjohann, W., Volwerk, M., Erkaev, N., Klecker, B., Lucek, E. A.,  
1058 Dandouras, I., André, M. and Khotyainstev, Y. (2009). Evolution of dipolarization in the near-  
1059 Earth current sheet induced by Earthward rapid flux transport. *Ann. Geophys.*, 27, 1743-  
1060 1754. doi:10.5194/angeo-27-1743-2009  
1061
- 1062 Ness, N. F. (1965). The Earth's Magnetic Tail. *J. Geophys. Res.*, 70 (13), 2989–3005.  
1063 doi:10.1029/JZ070i013p02989  
1064
- 1065 Newell, P. T., Sotirelis, T., Liou, K., Meng, C. -I. and Rich, F. J. (2007). A nearly universal solar  
1066 wind-magnetosphere coupling function inferred from 10 magnetospheric state variables. *J.*  
1067 *Geophys. Res.*, 112 (A1), A01206. doi: 10.1029/2006JA012025  
1068
- 1069 Nishitani, N., Ruohoniemi, J. M., Lester, M., Baker, J. B. H., Koustov, A. V., Shepherd, S. G.,  
1070 Chisham, G., Hori, T., Thomas, E. G., Makarevich, R. A., Marchaudon, A., Ponomarenko, P.,  
1071 Wild, J. A., Milan, S. E., Bristow, W. A., Devlin, J., Miller, E., Greenwald, R. A., Ogawa, T. and  
1072 Kikiuchi, T. (2019). Review of the accomplishments of mid-latitude Super Dual Auroral Radar  
1073 Network (SuperDARN) HF radars. *Progress in Earth and Planetary Science*, 6:27.  
1074 doi:10.1186/s40645-019-0270-5  
1075
- 1076 Ohma, A., Østgaard, N., Reistad, J. P., Tenfjord, P., Laundal, K. M., Moretto Jørgensen, T.,  
1077 Haaland, S. E., Krčelic, P. and Milan, S. (2019). Observations of Asymmetric Lobe Convection  
1078 for Weak and Strong Tail Activity. *J. Geophys. Res.: Space Physics*, 124 (12).  
1079 doi:10.1029/2019JA026773  
1080
- 1081 Pettigrew, E. D., Shepherd, S. G. and Ruohoniemi, J. M. (2010). Climatological patterns of  
1082 high-latitude convection in the Northern and Southern hemispheres: Dipole tilt  
1083 dependencies and interhemispheric comparisons. *J. Geophys. Res.*, 115, doi:  
1084 10.1029/2009JA014956.  
1085
- 1086 Petrukovich, A. A. (2011). Origins of plasma sheet B<sub>y</sub>. *J. Geophys. Res.*, 116 (A7), A07217.  
1087 doi:10.1029/2010JA016386  
1088
- 1089 Petrukovich, A. A., Baumjohann, W., Nakamura, R., Schödel, R., and Mukai, T. (2001). Are  
1090 earthward bursty bulk flows convective or field-aligned? *J. Geophys. Res.*, 106 (A10), 21,211-  
1091 21,215. doi:10.1029/2001JA900019  
1092
- 1093 Petrukovich, A. A., Baumjohann, W., Nakamura, R., Runov, A., and Balogh, A. (2005). Cluster  
1094 vision of the magnetotail current sheet on a macroscale. *J. Geophys. Res.*, 110 (A6), A06204.  
1095 doi:10.1029/2004JA010825  
1096
- 1097 Pitkänen, T., Hamrin, M., Norqvist, P., Karlsson, T., and Nilsson, H. (2013). IMF dependence  
1098 of the azimuthal direction of earthward magnetotail fast flows. *Geophys. Res. Lett.*, 40 (21),  
1099 5598-5604. doi:10.1002/2013GL058136  
1100

- 1101 Pitkänen, T., Hamrin, M., Norqvist, P., Karlsson, T., Nilsson, H., Kullen, A., Imber, S. M. and  
1102 Milan, S. E. (2015). Azimuthal velocity shear within an earthward fast flow: further evidence  
1103 for magnetotail untwisting? *Ann. Geophys.*, 33, 245-255. doi:10.5194/angeo-33-245-2015  
1104
- 1105 Pitkänen, T., Hamrin, M., Karlsson, T., Nilsson, H., and Kullen, A. (2017). On IMF  $B_y$ -Induced  
1106 Dawn-Dusk Asymmetries in Earthward Convective Fast Flows. In: Haaland, S. et al. (2017),  
1107 *Dawn-Dusk Asymmetries in Planetary Plasma Environments*, John Wiley and Sons, Inc., 107-  
1108 123.  
1109
- 1110 Pitkänen, T., Kullen, A., Laundal, K. M., Tenfjord, P., Shi, Q. Q. Park. J. -S., Hamrin, M., De  
1111 Spiegeleer, A., Chong, G. S. and Tian, A. M. (2019). IMF  $B_y$  Influence on Magnetospheric  
1112 Convection in Earth's Magnetotail Plasma Sheet. *Geophys. Res. Lett.*, 46 (21), 11,698-11,708.  
1113 doi:10.1029/2019GL084190  
1114
- 1115 Reistad, J. P., Østgaard, N., Tenfjord, P., Laundal, K. M., Snekvik, K., Haaland, S., Milan, S. E.,  
1116 Oksavik, K., Frey, H. U. and Grocott, A. (2016). Dynamic effects of restoring footprint  
1117 symmetry on closed magnetic field lines. *J. Geophys. Res.: Space Physics*, 121 (5),  
1118 015JA022058. doi:10.1002/2015JA022058  
1119
- 1120 Reistad, J. P., Østgaard, N., Laundal, K. M., Ohma, A., Snekvik, K., Tenfjord, P., Grocott, A.,  
1121 Oksavik, K., Milan, S. E. and Haaland, S. (2018). Observations of asymmetries in ionospheric  
1122 return flow during different levels of geomagnetic activity, *J. Geophys. Res.*, 123.  
1123 doi:10.1029/2017JA025051  
1124
- 1125 Rème, H., Bosqued, J. M., Sauvaud, J. A., Cros, A., Dandouras, J., Aoustin, C., Bouyssou, J.,  
1126 Camus, Th., Cuvilo, J., Martz, C., Médale, J. L., Perrier, H., Romefort, D., Rouzaud, J., d'Uston,  
1127 C., Möbius, E., Crocker, K., Granoff, M., Kistler, L. M., Popecki, M., Hovestadt, D., Klecker, B.,  
1128 Paschmann, G., Scholer, M., Carlson, C. W., Curtis, D. W., Lin, R. P., McFadden, J. P.,  
1129 Formisano, V., Amata, E., Bavassano-Cattaneo, M. B., Baldetti, P., Belluci, G., Bruno, R.,  
1130 Chionchio, G., Di Lellis, A., Shelley, E. G., Ghielmetti, A. G., Lennartsson, W., Korth, A.,  
1131 Rosenbauer, H., Lundin, R., Olsen, S., Parks, G. K., McCarthy, M. and Balsiger, H. (1997). The  
1132 Cluster Ion Spectrometry (CIS) Experiment. *Space Sci. Rev.*, 79, 303-350. doi:10.1007/978-  
1133 94-011-5666-0\_12  
1134
- 1135 Rong, Z. J., Barabash, S., Stenberg, G., Futaana, Y., Zhang, T. L., Wan, W. X., Wei, Y. and  
1136 Wang, X. -D. (2015). Technique for diagnosing the flapping motion of magnetotail current  
1137 sheets based on single-point magnetic field analysis. *J. Geophys. Res.: Space Physics*, 120 (5),  
1138 3462-3474. doi:10.1002/2014JA020973  
1139
- 1140 Runov, A. Nakamura, R., Baumjohann, W., Zhang, T. L., Volwerk, M., Eichelberger, H. -U. and  
1141 Balogh, A. (2003). Cluster observations of a bifurcated current sheet. *Geophys. Res. Lett.*, 30  
1142 (2), 1036. doi:10.1029/2002GL016136  
1143
- 1144 Runov, A., Angelopoulos, V., Sergeev, V. A., Glassmeier, K. -H., Auster, U., McFadden, J.,  
1145 Larson, D. and Mann, I. (2009). Global properties of magnetotail current sheet flapping:  
1146 THEMIS perspectives. *Ann. Geophys.*, 27, 319-328. doi:10.5194/angeo-27-319-2009  
1147

Deleted: ¶

Deleted: ¶

- 1150 Ruohoniemi, J. M. and Baker, K. B. (1998). Large-scale imaging of high-latitude convection  
1151 with Super Dual Auroral Radar Network HF radar observations. *J. Geophys. Res.*, *103* (A9),  
1152 20,797-20,811. doi:10.1029/98JA01288  
1153  
1154 Ruohoniemi, J. M. and Greenwald, R. A. (1996). Statistical patterns of high-latitude  
1155 convection obtained from Goose Bay HF radar observations. *J. Geophys. Res.*, *101* (A10),  
1156 21,743-21,763. doi:10.1029/96JA01584  
1157  
1158 Sergeev, V. A., Angelopoulos, V., Gosling, J. T., Cattell, C. A., and Russell, C. T. (1996).  
1159 Detection of localized, plasma-depleted flux tubes or bubbles in the midtail plasma sheet. *J.*  
1160 *Geophys. Res.*, *101* (A5), 10,817 – 10,826. doi:10.1029/96JA00460  
1161  
1162 Sonnerup, B. U. Ö, and Cahill Jr, L. J. (1967). Magnetopause structure and attitude from  
1163 Explorer 12 observations. *J. Geophys. Res.*, *72* (1), 171-183.  
1164 doi:10.1029/JZ072i001p00171  
1165  
1166 Sonnerup, B. U. Ö and Scheible, M. (1998). Minimum and Maximum Variance Analysis. In:  
1167 Paschmann, G. and Daly, W. (1998), *Analysis Methods for Multi-Spacecraft Data*, pp 185-  
1168 220, ESA Publications Division, Noordwijk, Netherlands.  
1169  
1170 Tenfjord, P., Østgaard, N., Snekvik, K., Laundal, K. M., Reistad, J. P., Haaland, S., and Milan, S.  
1171 E. (2015). How the IMF  $B_y$  induces a  $B_y$  component in the closed magnetosphere and how it  
1172 leads to asymmetric currents and convection patterns in the two hemispheres. *J. Geophys.*  
1173 *Res.: Space Physics*, *120* (11), 9368-9384. doi:10.1002/2015JA021579  
1174  
1175 Tenfjord, P., Østgaard, N., Strangeway, R., Haaland, S., Snekvik, K., Laundal, K. M., Reistad, J.  
1176 P. and Milan, S. E. (2017). Magnetospheric response and reconfiguration times following  
1177 IMF  $B_y$  reversals. *J. Geophys. Res.: Space Physics*, *122* (1), 417-431.  
1178 doi:10.1002/2016JA023018  
1179  
1180 Thomas, E. G. and Shepherd, S. G. (2018). Statistical Patterns of Ionospheric Convection  
1181 Derived From Mid-Latitude, High-Latitude and Polar SuperDARN HF Observations. *J.*  
1182 *Geophys. Res.: Space Physics*, *123* (4), 3196-3216. doi:10.1002/2018JA025280  
1183  
1184 Tsyganenko, N. A. and Andreeva, V. A. (2015). A forecasting model of the magnetosphere  
1185 driven by an optimal solar wind coupling function. *J. Geophys. Res.*, *120* (10), 8401-8425.  
1186 doi:10.1002/2015JA021641  
1187  
1188 Volwerk, M., Zhang, T. L., Glassmeier, K. -H., Runov, A., Baumjohann, W., Balogh, A., Rème,  
1189 H., Klecker, B. and Carr, C. (2008). Study of waves in the magnetotail region with cluster and  
1190 DSP. *Advances in Space Research*, *41* (10), 1593-1597. doi:10.1016/j.asr.2007.04.005.  
1191  
1192 Wei, X. H., Cai, C. L., Cao, J. B., Rème, H., Dandouras, I., and Parks, G. K. (2015). Flapping  
1193 motions of the magnetotail current sheet excited by nonadiabatic ions. *Geophys. Res. Lett.*,  
1194 *42*, 4731-4735. doi:10.1002/2015GL064459  
1195

- 1196 Wei, Y. Y., Huang, S. Y., Rong, Z. J., Yuan, Z. G., Jiang, K., Deng, X. H., Zhou, M., Fu, H. S., Yu,  
1197 X. D., Xu, S. B., He, L. H. and Deng, D. (2019). Observations of Short-period Current Sheet  
1198 Flapping Events in the Earth's Magnetotail. *The Astrophysical Journal Letters*, 874, 7pp.  
1199 doi:10.3847/2041-8213/ab0f28/pdf.  
1200  
1201 Wu, M., Lu, Q., Volwerk, M., Vörös, Z., Ma, X., and Wang, S. (2016). Current sheet flapping  
1202 motions in the tailward flow of magnetic reconnection. *J. Geophys. Res.*, 121 (8), 7817-7827.  
1203 doi:10.1002/2016JA022819  
1204  
1205 Zhang, L. Q., Baumjohann, W., Wang, C., Dai, L., and Tang, B. B. (2016). Bursty bulk flows at  
1206 different magnetospheric activity levels: Dependence of IMF conditions. *J. Geophys. Res.*,  
1207 121 (9), 8773-8789. doi:10.1002/2016JA022397  
1208  
1209